ChemPubSoc Europe

https://doi.org/10.1002/ejic.201800146

EurJIC European Journal of Inorganic Chemistry

Microreview

Aspects of Bubbly Flows for Chemists | *Very Important Paper* |

CLUSTER ISSUE

VIP

Reaction Systems for Bubbly Flows

Melanie Paul,[a] Florian Strassl,[a] Alexander Hoffmann,[a] Marko Hoffmann,[b] Michael Schlüter,[b] and Sonja Herres-Pawlis*[a]

Abstract: Reactive bubbly flows are at the heart of multiphase flows which are a major topic in chemical engineering since many bulk chemicals are produced in bubbly flows. However, the factors determining product yield and selectivity are often subject of complicated mass transfer effects. Herein, we describe the latest developments in the detection of mass transfer effects in bubbly flows. Coordination chemistry has given new impulses to this topic due to the possibility to synthesise tailored complex systems for the detection of O_2 and NO with various time- and space-resolved techniques. For each chemical reaction system, a background section is summarised to allow the reader to get an overview of the different systems.

1. Introduction

The chemical transformation of substances with high yield and high selectivity is one of the most important tasks in chemical engineering. For the synthesis of many bulk chemicals, gaseous starting compounds have to be brought in close contact with a continuous liquid phase, e.g. in oxidation, hydrogenation and chlorination reactions. Oxygen is the cheapest and most atom-economic oxidant and thus, a direct oxygenation using air is preferable to any other method from a chemical point of view. In the 1960s, bubble column reactors have been developed for this purpose which enable large volumes and long residence times with intensive mixing. In the 1980s, bubble columns with zones of defined mixing and a guided liquid stream (e.g. in loop reactors) have been applied.

Since then, it was shown that chemical reactions are influenced by mixing in different time and space scales. Reactive bubbly flows show here a large potential for optimisation since additional mass transfer limitations through phase interfaces and boundaries occur. Unfortunately, scale overlapping transfer processes with coupled reaction cannot yet be sufficiently described such that the predictive power of yield and selectivity is extremely limited. In the last years, some progress has been made in miniaturised reactors, new measurements techniques with unprecedented resolution in space and time as well as numerical simulations. These developments in chemical engineering, numerical mathematics, physics and chemistry are often rather separated from each other. The DFG priority programme 1740 comprises groups from all these fields to enable a transdisciplinary approach for the combination of new chemical reaction networks for bubbly flows which are investigated by new physical techniques and simulated by new theoretical methods as well. In this review, we summarise recent developments in the field of reactive bubble flows with special focus on the reactive systems.

The final goal is the full understanding of the hydrodynamic behaviour of bubble swarms including mass transfer of a selected gaseous component and concentration gradients in the swarm as well as the competition between mass transfer and chemical reaction. The complexity of a bubble swarm is enormous; hence, a reduction of dimensions is often used to simplify the setup for reasonable measurement resolution in space and time as well as efficient numerical simulation. Examples for such apparatus are small bubble columns with single bubbles but still here, the bubble has the possibility to move in all directions. The next reduction is a 2D Hele–Shaw cell in which the bubble is flat between two glass windows. Even more reduction is possible in a so-called Taylor flow where a single bubble streams in a capillary. These setups are discussed in section 2.1.

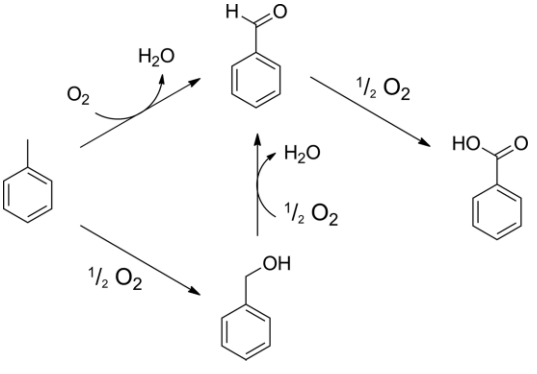

Scheme 1. Reaction scheme of the oxidation of toluene.[6]

[a] *Institute of Inorganic Chemistry, RWTH Aachen University, Landoltweg 1, 52074 Aachen, Germany*
E-mail: sonja.herres-pawlis@ac.rwth-aachen.de
http://www.bioac.ac.rwth-aachen.de/
[b] *Hamburg University of Technology, Institute of Multiphase Flows, Eißendorfer Straße 38, 21073 Hamburg, Germany*
ORCID(s) from the author(s) for this article is/are available on the WWW under https://doi.org/10.1002/ejic.201800146.

Several studies reported in the last years that for large-scale bulk chemical production a relationship between product quality and local mass transfer processes is present. However, these relationships could not be sufficiently explained or described until today.[1–5] Examples for such reactions are the cumene oxidation,[2] toluene oxidation (Scheme 1)[6] and also chlorination reactions.[7]

The actual models for the description of local mass transfer at phase boundaries are based on the two-film theory of Lewis and Whitman[8] and the penetration theory of Higbie[9] (Figure 1). Following the two-film theory, a laminar film is formed on both sides of the interface which is regarded as main resistance for mass transfer. It is then postulated that in these boundary layers no mixing occurs and that the mass transfer is accomplished purely by diffusion. In the core of the gas and liquid phase, convective movements of the fluids lead to a fast balancing of concentrations. The mass transfer at the interface is driven by a non-equilibrium of concentration and Henry's law

Melanie Paul received her B.S. degree in Chemistry in 2015 and pursued her graduate studies at RWTH Aachen University. In autumn 2017, she finished her master thesis in the field of bioinspired reaction systems with copper complexes. She is currently working on her Ph.D. in inorganic chemistry at RWTH Aachen University under the supervision of Prof. Dr. S. Herres-Pawlis. Her thesis investigations are focused on the activation of dioxygen with copper(I) complexes inspired by tyrosinase.

Florian Strassl studied Chemistry at RWTH Aachen University. After finishing his master thesis in technical chemistry in 2013, he worked as a research assistant in process engineering in Aachen. Afterwards he began his PhD in the work group of Prof. Dr. Herres-Pawlis in inorganic chemistry. His research focuses on the topic of copper complexes for the activation of dioxygen in bubbly flows.

Alexander Hoffmann is holding a permanent position in the Herres-Pawlis group at RWTH Aachen University for advanced spectroscopy, density functional calculations and X-ray crystallography. He studied Chemistry at the University of Paderborn and finished his PhD thesis at TU Dortmund in 2011 on the coordination chemistry of late transition metals for catalysis and bioinorganic chemistry. Then, he moved to LMU Munich and turned to the theoretical description of N-donor transition metal systems with focus on copper–dioxygen chemistry. In 2013, he was awarded with the Römer-Postdoc Prize.

Marko Hoffmann is a senior engineer and group leader for the subject "Multi-scale Transport Processes" at the Institute of Multiphase Flows at Hamburg University of Technology (TUHH). He studied Energy Engineering and Process Engineering at TU Berlin. He worked as a process engineer in two different companies and as a doctoral researcher at the University of Bremen, Institute of Environmental Process Engineering, where he received his doctoral degree in 2012.

Michael Schlüter studied Mechanical and Process Engineering at the University of Bremen and continued as PhD student at the Institute of Environmental Process Engineering. He received his PhD in 2001 at the University of Bremen and headed afterwards the group of "Multiphase Reactors" at the same institution. In 2009 he received the Venia Legendi in "Process Engineering" with the habilitation treatise "Multiscale Transport Processes in Multiphase Flows". Since 2009 Prof. Schlüter owns the Chair of "Fluid Mechanics for Multiphase Systems" at the Hamburg University of Technology and is head of the Institute of Multiphase Flows. Prof. Schlüter is coordinator of the DFG Priority Program 1740 "Reactive Bubble Columns" and President of the Working Party "Multiphase Fluid Flow" in the European Federation of Chemical Engineering.

Sonja Herres-Pawlis leads since 2015 the Chair of Bioinorganic Chemistry at RWTH Aachen University. She studied Chemistry at Paderborn, Germany, and Montpellier, France. After her PhD thesis (Paderborn 2005), Postdoc (Stanford University) in bioinorganic copper–dioxygen chemistry, and habilitation on sustainable polymerisation catalysts with Venia Legendi in inorganic chemistry at TU Dortmund in 2012, she worked as associate professor for coordination chemistry at LMU Munich. She received the Innovation Prize of the state of Northrhine-Westphalia and the Arnold-Sommerfeld Prize of the Bavarian Academy of Arts and Sciences. She was speaker of the interdisciplinary DFG Research Unit FOR1405 and is member of the programme committee of the DFG Priority Program 1740 "Reactive Bubble Columns".

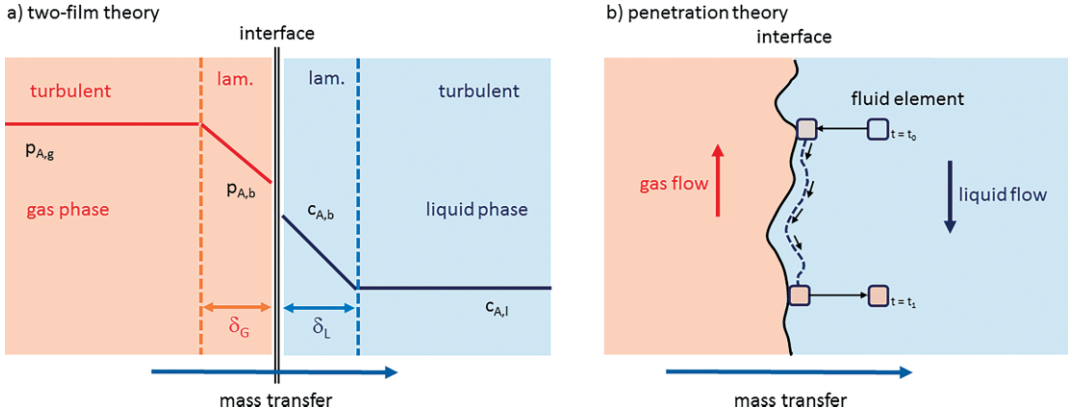

Figure 1. Mass transfer following the (a) two-film theory ($p_{A,g}$: partial pressure in gas phase, $p_{A,b}$: partial pressure in gas boundary layer, $c_{A,l}$: concentration in liquid phase, $c_{A,b}$: concentration in liquid boundary layer) and (b) the penetration theory.

is valid.[10] During mass transfer from gas phase to liquid phase, a component A diffuses through the boundary layer δ_g to the interface and from there through the second boundary layer δ_L. The driving force of the mass transfer corresponds to the concentration gradient between the core of the phases and the interface. The molecular mass transfer within the laminar boundary layer is given by the first Fick's law whereas the liquid-phase mass transfer coefficient is dictated by the diffusion coefficient D and the liquid boundary layer thickness δ_L. The assumption of a laminar boundary layer as film with a thickness δ is compared to real gas–liquid systems a rough simplification. Higbie has introduced the penetration model for the non-steady state mass transfer where an exchange of fluid elements is taken into account (Figure 1b). At the time $t = t_0$ a fluid element is transported from the core flow to the interface and remains there until $t = t_1$. During the residence time t_m, a diffusion of the gas component into the fluid element takes place. At $t = t_1$ the fluid element is transported back into the bulk flow.

In order to obtain space- and time-resolved data, multiple techniques such as fluorescence spectroscopy, Raman spectroscopy and tomography have been applied. The central task is focused on the visualisation of the concentration profile in the liquid boundary layer, and consumption or formation of substances to allow the calculation of the reaction kinetics in competition with the mass transfer through the phase interface. The gaseous component has to cross the phase boundary and is then consumed in a chemical reaction (Figure 2). This behaviour shall be monitored and simulated.

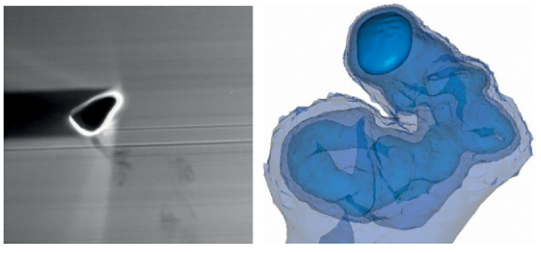

Figure 2. Mass transfer of a freely rising bubble; left: experimentally,[11] right: in simulation.[12] Reproduced with permission. Copyright 2012 Elsevier.

This is complicated by the temperature dependence of the consumption of the gaseous component (Figure 3).[13] It was found that different sectors of a rising bubble contribute differently to the mass transfer. Moreover, the wake turned out to be not homogeneously mixed.

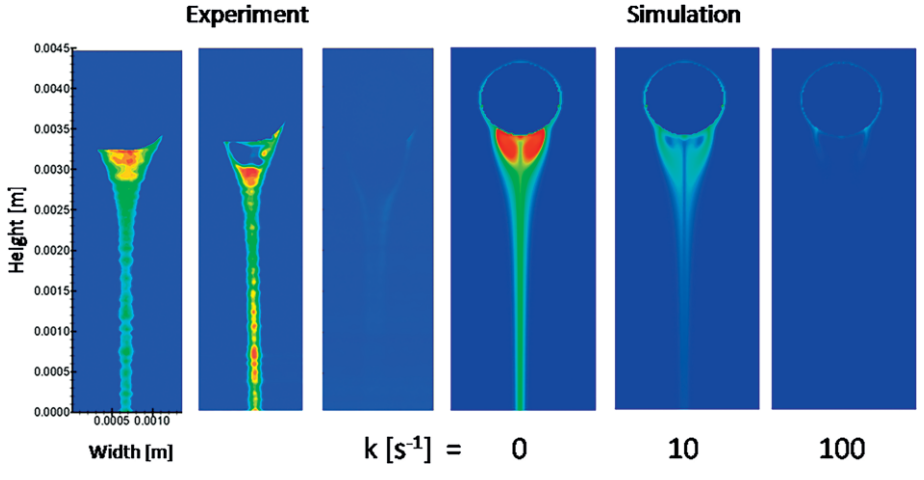

Figure 3. Mass transfer of a linear rising O_2 bubble for the consumption of the gaseous component by the sulfite oxidation (left: experiment (1) without reaction, (2) 15 °C, (3) 26 °C; right: simulation at different reaction rates). Reproduced from ref.[13]

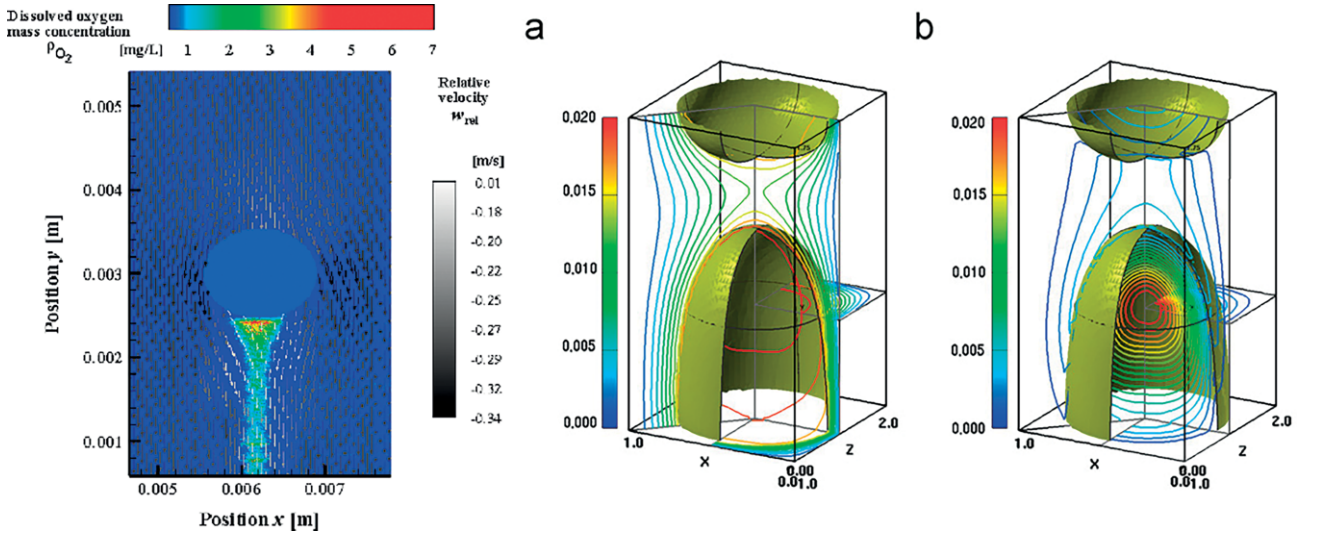

Figure 4. Left: Simultaneously captured velocity and concentration field of a freely rising bubble,[14] right: Simulated concentration field in 3D.[15] Reproduced with permission. Copyright 2012 Chemical Society of Japan and 2009 Elsevier.

In the best case, a detailed concentration and velocity field is obtained by combination of measurements and simulations (Figure 4).

In catalysis, the knowledge of the intrinsic kinetics (kinetics without mass transfer limitation, i.e. reaction between two miscible liquid phases or an already dissolved gas in a liquid phase) is the key for efficient operation of bubble columns. As important is the so-called enhancement factor. In best case, a reaction which consumes the gas speeds up the mass transfer (*enhancement*).[10] The enhancement factor *E* describes the mass transfer acceleration due to a chemical reaction by the ratio of the mass streams in the reactive and non-reactive case. Technically, the Hatta number *Ha* is also used which denotes the ratio of intrinsic reaction rate and mass transfer rate. It is related to the enhancement factor whereas *D* is the diffusion coefficient, *k* the reaction rate constant, k_L the liquid-phase mass transfer coefficient and *n* the reaction order:

$$E = \frac{Ha}{\tanh Ha} \text{ with } Ha = \frac{1}{k_L}\sqrt{\frac{2}{n+1}\cdot k \cdot D \cdot c^{n-1}}$$

A long-term objective in this topic is the predictive description of sequential reactions. This comprises purely consecutive reactions but more importantly, competitive-consecutive reactions, in which the product can react again with the transferred gaseous compound (Scheme 2). Here, the yield and selectivity of the reaction products R and S depend highly on the mixing efficiency and the mass transfer coefficients. An example is the toluene and cumene oxidation.[2,6]

Consecutive reaction:

$$A + B \longrightarrow R \longrightarrow S$$

Competitive-consecutive reaction:

$$A + B \longrightarrow R$$
$$R + B \longrightarrow S$$

Scheme 2. General formalism of consecutive and competitive-consecutive reactions.

Historically, for the study of mass transfer reactions non-reactive systems have been used to understand solely the mass transfer without following reaction or enhancement. In the next step, non-toxic aqueous systems with high environmental relevance such as CO_2 adsorption into water have been investigated (see Section 2). Further, the adsorption of O_2 has been studied without and with chemical reaction as indicator (see Section 3.1 and 3.2). In the next generation, the request for real reaction networks grew which might be tailored to the detection method – in best case combined with competitive-consecutive reaction patterns. Here, coordination chemistry offers an ideal playground to use gas-consuming reactions with colourful products with characteristic Raman and/or IR features or fluorescence behaviour which enables these studies. Additionally, reaction kinetics for many reactions can be tuned for the applications in Taylor flows and similar apparatus. Recent developments in Cu/O_2 and Fe/O_2 chemistry (sections 3.3 and 3.4) and Fe/NO chemistry (see Section 4) are summarised in the following since these three topics have gained considerable attention at the interface between chemistry and chemical engineering.

2. Systems with CO_2

To analyse the different properties of bubbles and bubble column reactors, an easy to handle system is needed. For further progress in evaluating the chemical differences when varying the solvent or the system, which is activated or changed by the gas, the basic environment of the actual multiphase system should be investigated first. Interesting factors like the bubble velocities, sizes and rising behaviour is usually measured in a water/CO_2 system.[16–18]

Water/CO_2 is a very common system for such investigations in chemical engineering although the reaction is rather simple. Water is a non-hazardous solvent which is cheap and available in large amounts. The gas carbon dioxide is neither flammable, explosive nor toxic and therefore also suitable for basic tests.

When CO_2 gas flows through the liquid phase it partially dissolves and changes the pH value. The change of the pH can be further enhanced by a NaOH solution as liquid phase (Scheme 3). This effect is utilised by different spectroscopic methods to analyse bubble dynamics.[19–21] Furthermore, different detection techniques use different setups with varying dimensionality. The following section introduces the reader compactly into typical setups used in fluid mechanics, ranging from the single bubble over 2D bubbles to small bubbles columns.

$$CO_{2(aq)} + OH^- \rightleftharpoons HCO_3^-$$

$$HCO_3^- + OH^- \rightleftharpoons CO_3^{2-} + H_2O$$

Scheme 3. Reaction of CO_2 in NaOH solution.

2.1 Taylor Flow Bubbles

The simplest setup to study the reaction between a bubble and a liquid phase is a so-called Taylor flow, a captured bubble in a defined capillary.[22] Usually the bubbles are either moving through the capillary or the Taylor bubbles are fixed at a certain position through a counter-current flow. In special kinds of Taylor flows, a series of defined bubbles flows through the capillary. Mass transfer monitoring in Taylor flows can be accomplished by Raman spectroscopy, fluorescence spectroscopy, diverse holographic techniques etc. depending on the speed of the bubbles and the chemical system. Selected examples are discussed below.

The combination of Raman and Mach-Zehnder holography led to images of CO_2 bubbles in a millimetric channel setup (Figure 5).[23] A rectangular channel with a cross-section of 2×2 mm provided optical access to the Taylor flow. Two systems were measured: a non-reactive system (cyclohexane, methanol and air) and a reactive system (NaOH solution and CO_2). Through measurement at different optical axes and synchronisation with Raman spectroscopy, visualisations of bubbles in a 3D space were achieved.

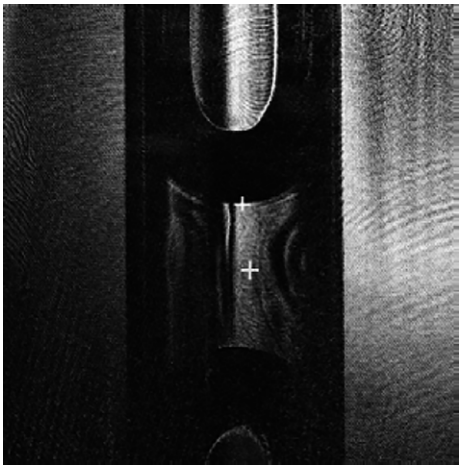

Figure 5. Combined Raman spectroscopy and Mach-Zehnder holography: distance between the measuring points (lowest point of bubble and laser spot) where the concentration was measured. Reproduced from ref.[23]

Kastens et al. produced reactive Taylor flow bubbles using CO_2 in a vertical glass channel with a length of 300 mm (Figure 6).[24]

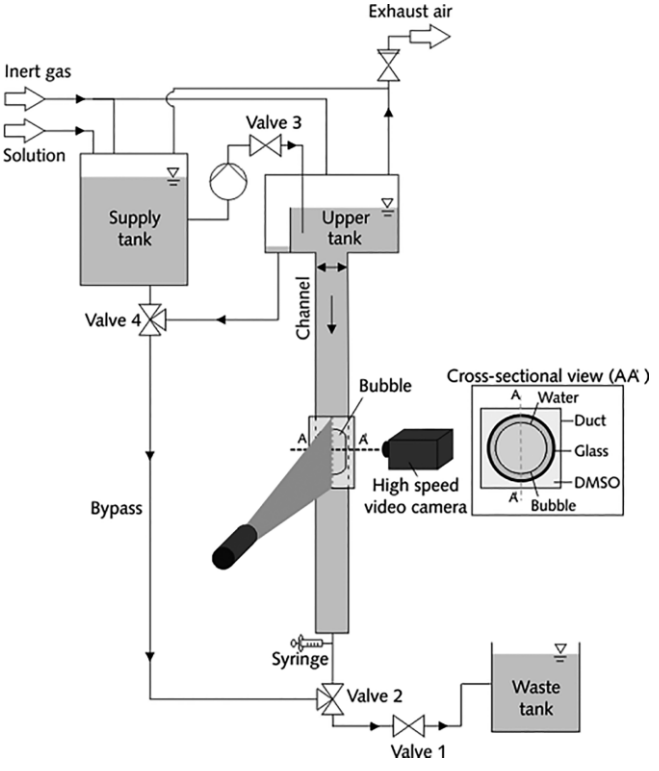

Figure 6. Taylor flow experimental setup. Reproduced from ref.[24]

They tested CO_2 bubbles in deionised water rising with a constant velocity and in counter-current flow. The counter-current flow holds the bubble at the point of the high-speed camera through the volume flow of a downflowing liquid, which is adjusted to the velocity of the bubble. To mark the CO_2 containing phase in the liquid for laser-induced fluorescence (LIF)

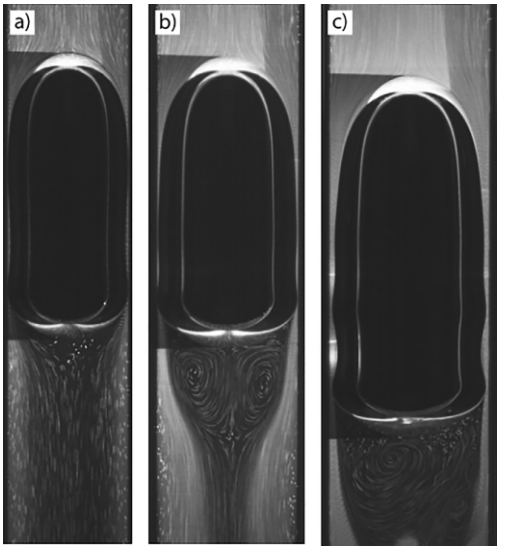

Figure 7. Average images of the wake structure behind Taylor bubbles in counter-current flow in different channel diameters. (a) D = 6 mm, (b) D = 7 mm, (c) D = 8 mm. Reproduced from ref.[24]

measurements, fluorescein was used. In this method, a light-section by a strong laser allows the space- and time-resolved detection of fluid elements. The fluorescence of fluorescein depends on the pH value of the solution which is influenced by CO_2.[25] With the LIF measurements, they were able to visualise and characterise the wake structures in terms of physisorption, chemisorption and rise velocities (Figure 7). Moreover, measurements of the local flow field and wake structure were performed by means of particle image velocimetry (PIV).

2.2 Bubbles in a Two-Dimensional Environment

A more advanced analysis method for the CO_2/water system in terms of bubble movement is a Hele–Shaw cell.[16] A rising bubble with a cylindrical shape is produced between two glass walls with a gap of 1 mm. Through these confined conditions, only the two-dimensional dynamics which have less variables than freely rising bubbles are evaluated. The water contains fluorescein which is quenched by decreasing pH. The used spectroscopic method is planar laser-induced fluorescence (PLIF, Figure 8). PLIF is a widely used method for two-dimensional measurements of dissolved gas transport in aqueous environments.[26–28] The aim of the experiments was to characterise the propagating CO_2-rich boundary layer and the bubble dissolution dynamics. They achieved a visual characterisation of the CO_2 propagation and demonstrated good comparability of results with regard to numerical simulations (Figure 9).

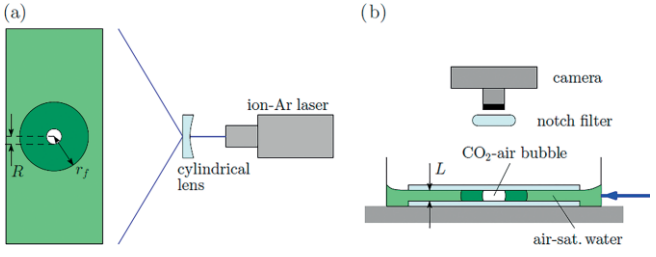

Figure 8. (a) Plan view and (b) side view of the experimental setup. PLIF revealed a CO_2-containing region [dark green enclosed by $r_f(t)$] propagating radially outward from the dissolving cylindrical bubble of radius $R(t)$.[16] Reproduced with permission. Copyright 2017 American Physical Society.

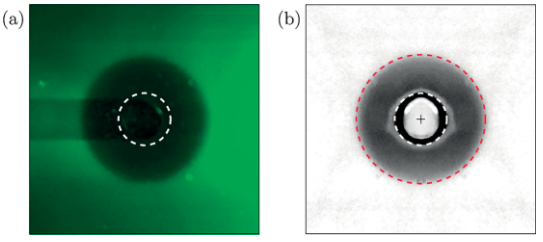

Figure 9. Comparison of (a) a raw image and (b) a processed image. The white dotted circle marks the initial bubble circumference, while the red dotted circle marks the front position.[16] Reproduced with permission. Copyright 2017 American Physical Society.

2.3 Bubbles in a Bubble Column Setup

Rising bubbles in a bubble column can also be measured by a wire-mesh sensor as shown by Kipping et al.[17] A setup was built to analyse changes in conductivity at different heights of the column with CO_2 bubbles rising in the column through the wire-mesh measurement planes (Figure 10). This conductivity

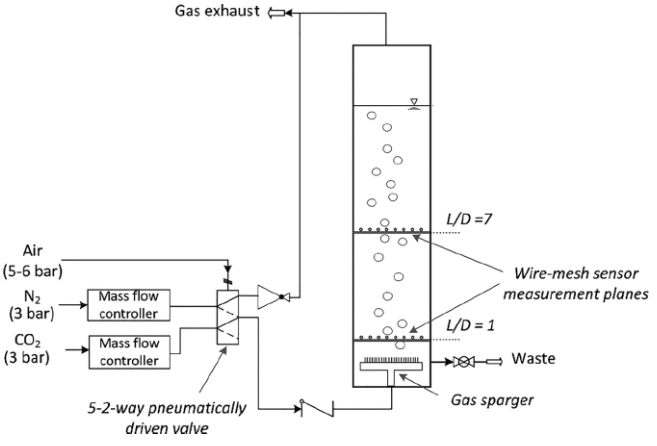

Figure 10. Schematic drawing of the experimental bubble column setup. Reproduced from ref.[17]

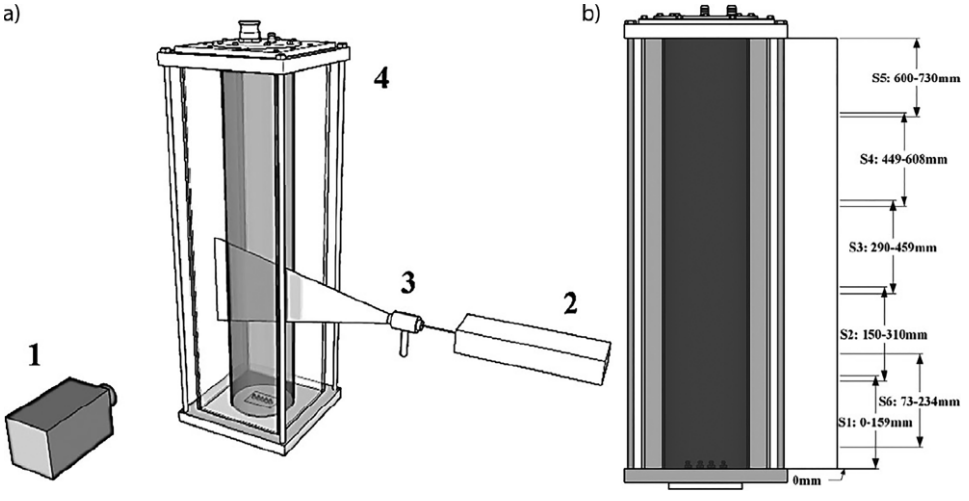

Figure 11. Experimental setup for PIV (a) with high-speed camera (1) high-speed laser (2), light-sheet optics (3), bubble column (4); (b) measurement windows. Reproduced from ref.[18]

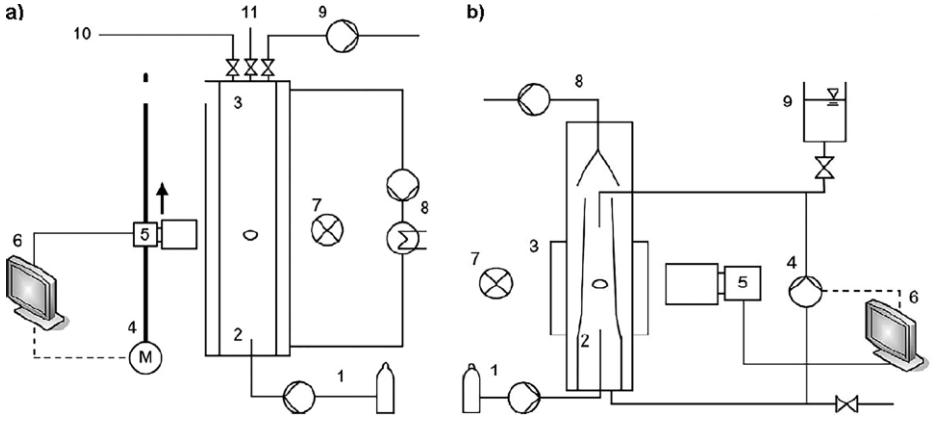

Figure 12. (a) Rising bubble test cell (b) counter-current flow cell. Reproduced from ref.[33]

changes occur through the reaction shown in Scheme 3. An increase of consumption rate with increasing gas superficial velocity and initial concentration was observed.

The rising bubbles in a bubble column were also analysed by a high-speed PIV camera.[18,29,30] The column had a diameter of 0.14 m and a filling height of 0.73 m and was made from acrylic glass with a thickness of 4 mm (Figure 11).

Merker et al. evaluated single bubbles in bubble columns with a rising bubble test cell and a counter-current flow test cell (Figure 12), following the works performed by Tsuchiya in 1997 and 2003.[31–33]

The rising bubble test cell consisted of high-speed cameras examining a single bubble. The cameras rose with the same speed as the bubble and followed its wake structure with the second camera. This facilitates to follow and analyse the bubble rising dynamics. In the second setup a counter-current flow was applied to hold the bubble in the column at a certain point having a fixed camera pointing at it. This setup allowed the shrinking, and therefore mass transfer effects of the gas and liquid phases, to be evaluated. In the shown study CO_2 and water were used as first test system, followed by the chemical system of Fe/NO (see section 4). Recently, Kong et al. introduced a more advanced dual emission LIF technique to further increase the obtained data on the mass transfer process in bubbly flows.[34]

3. Systems with O_2

O_2 is known as oxidising agent for many processes in nature. It is also actively used in the industry for oxidising substrates with bubble columns.[2,4] To use O_2 in bubble columns, researchers often use simple systems, where active species change their (spectroscopic) properties when reacting with O_2 but without a very complex reaction. This includes that often only O_2 in air is used as gaseous phase. As liquid phase many groups use water or water mixtures. In the study of Laupsien et al. the influence of the viscosity of the liquid phase was investigated in a bubble column with air as gaseous phase.[35]

The research in the O_2 testing environments is already closer to industrial processes than using CO_2, since O_2 oxidises substrates. The chemical systems used can be divided in three groups: (1) dying agents that change colour with O_2, (2) fluorescence agents that are quenched with O_2, (3) complexes that react with O_2 with colour or fluorescence change. These groups will be discussed in section 3.

3.1 Indicator dyes and Ruthenium complexes

One of the most frequently used dyes for applications with O_2 is rhodamine in combination with different monitoring techniques. Bork et al.[29] introduced the LIF techniques for gas–liquid systhems with rhodamine, and Mühlfriedel et al. used a similar technique for a liquid–liquid system.[36] Lindken and Merzkirch presented a PIV technique for measuring bubbly flows with rhodamine as fluorescent tracer.[37] It consisted of the most frequently used PIV techniques in multiphase flows: measurements with fluorescent tracers, shadowgraphy and digital phase separation with masking technique.[38] With shadowgraphy a shadow image of the gas bubbles could be recorded and their velocities were determined.

The colour of the dyes usually changes from colourless to an intense colour when oxidised or reduced. Methylene blue is blue when oxidised and colourless in the reduced state but has slow kinetics for fast reactions like a bubble rise.[39,40] Resazurin is a well-known dye that changes colour from blue (not fluorescent) to pink resorufin (highly fluorescent) when reduced (Figure 13).[41,42] Resorufin is then reduced to dihydroresorufin by itself. The advantage of this system is that both colorimetric and fluorescent-sensitive measurements are possible.

The reduction is catalysed by the oxidation of glucose to gluconate in the presence of sodium hydroxide (Scheme 4).

The air bubbles flow through a millimetric channel and are analysed with a high-speed camera (Figure 14). The images were evaluated with the colorimetric method, which means that different colour intensities represent different concentrations of the dye and therefore O_2.

Dietrich et al. were able to calculate air–liquid mass transfer coefficients. Recently, they used a column setup to estimate the mass transfer coefficients of free rising bubbles.[42] Yang et al. used the same system to analyse bubbles in microchannels and focus on the gas–liquid mass transfer at the bubble formation stage.[43] Krieger et al. found indigo carmine to be an efficient

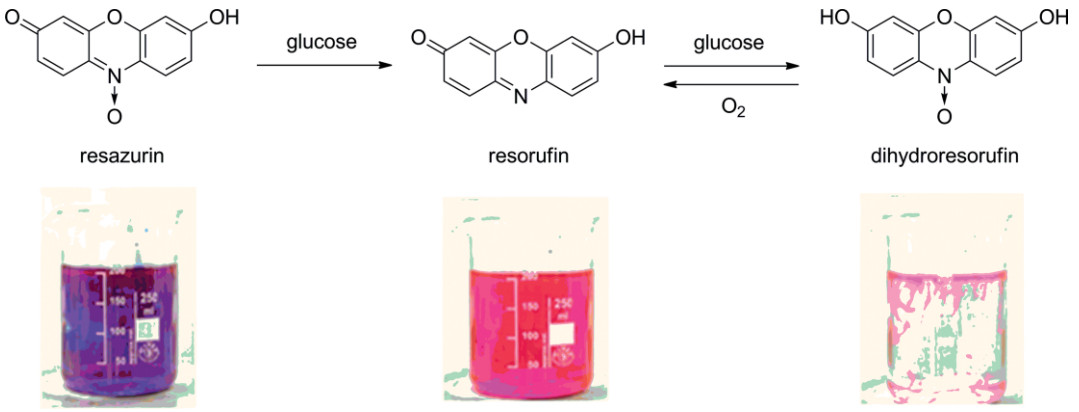

Figure 13. Reaction of resazurin to resorufin and dihydroresorufin.[41,42] Reproduced with permission. Copyright 2013 Elsevier.

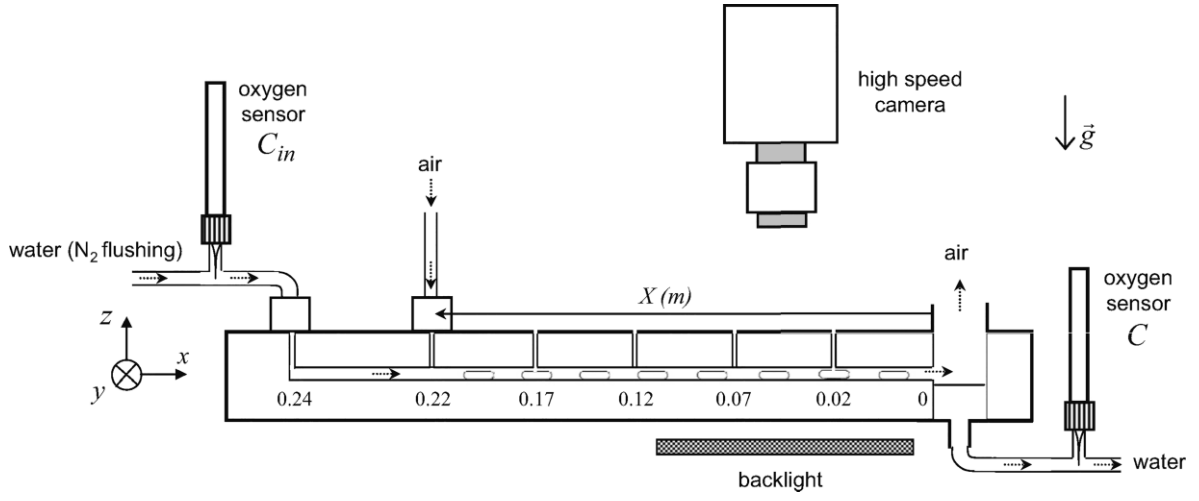

Figure 14. Reaction setup of colourimetric measurements.[41] Reproduced with permission. Copyright 2013 Elsevier.

$$HOCH_2(CHOH)_4CHO + 3\,OH^- \longrightarrow HOCH_2(CHOH)_4COO^- + 2\,H_2O + 2\,e^-$$

glucose — gluconate

Scheme 4. Oxidation of glucose to gluconate.[41]

dye. Leuco-indigo carmine was oxidised to keto-indigo carmine with oxygen and was subsequently reduced by glucose.[44]

The most effective fluorescent tracers for oxygen/water measurements, capable to be analysed with PLIF are ruthenium phenanthroline complexes (Figure 15).[45–49] Oxygen bubbles were investigated with LIF in a Taylor flow setup (see section 2.1) with tris-(1,10-phenanthroline)ruthenium(II) chloride.[38]

Dani et al. developed a non-invasive technique using PLIF and the Ru complex tris-(4,7-diphenyl-1,10-phenanthroline)-ruthenium(II) perchlorate to determine the oxygen concentration.[45] Around 17 % ethanol was added to the water solution to guarantee a fully dissolved complex. Oxygen quenches the fluorescence of the Ru complex and the fluorescence intensity was found to be proportional to the concentration of the dye. Roudet et al. used the fluorescence system to examine the patterns in the wakes of the oxygen bubbles.[48] They focused on the mass transfer mechanisms of two different regions: the flow

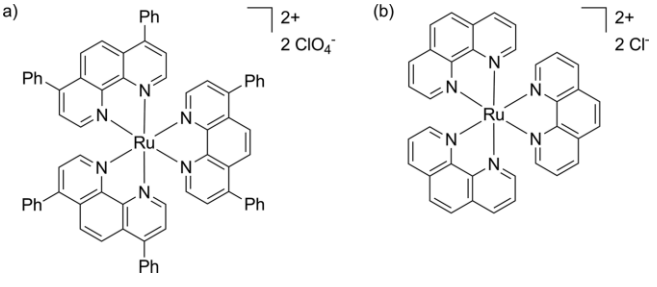

Figure 15. (a) Tris-(4,7-diphenyl-1,10-phenanthroline)ruthenium(II) perchlorate and (b) tris-(1,10-phenanthroline)ruthenium(II) chloride.

around a bubble with the two thin liquid films between the bubble and the cell wall, as well as an external high Reynolds number in-plane flow surrounding the bubble. This experimental setup was similar to a Hele–Shaw cell, which was also used for investigating oxygen bubbles.[49] They obtained PLIF images that show the wake structures around the flattened bubble (Figure 16).

Kück et al. analysed single bubbles in a 100 mm wide and 2 m high bubble column with combined PIV-LIF measurements

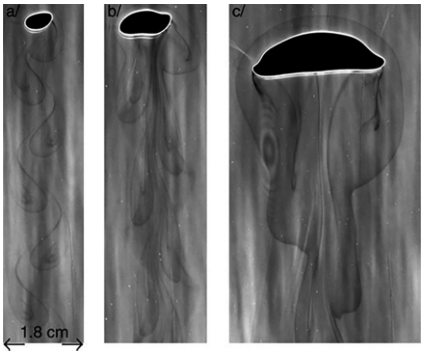

Figure 16. PLIF images of bubbles in Hele–Shaw cell; O_2 dissolved in the liquid field is revealed in the darker regions due to the quenching of the dye fluorescence. Reproduced from ref.[48]

with optional counter-current flow with the fluorescent tracer tris-(1,10-phenanthroline)ruthenium(II) chloride.[46,50] Besides water, they tested carboxymethyl cellulose as reaction medium. Through the higher viscosity a different behaviour of bubble wakes, velocity and movement was observed. In their measurement, they analysed the concentration fields around a freely rising bubble in a 3D environment (Figure 17).

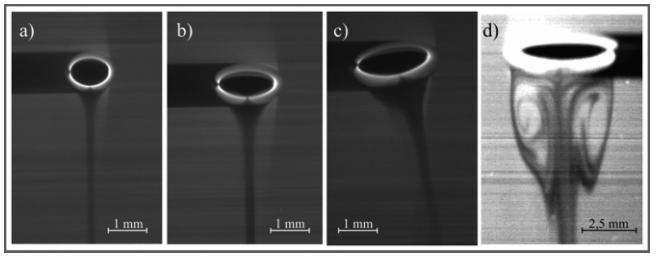

Figure 17. LIF images of differently sized oxygen bubbles; (a) d_e = 1.3 mm, (b) d_e = 1.7 mm, (c) d_e = 2.1 mm in water/oxygen, (d) d_e = 6 mm in carboxymethyl cellulose/O_2. Reproduced from ref.[46]

Huang and Saito analysed the effects of surface contamination on the bubble and wake structures with 3D LIF images and the fluorescent tracer HPTS (8-hydroxypyrene-1,3,6-trisulfonic acid trisodium salt).[51,52]

3.2 Sulfite/Sulfate

Oxygen mass transfer is also a critical process in the reaction from sulfite to sulfate. For instance, oxygen scavenging by sulfite compounds is an important task to inhibit corrosion in industrial water circuits. In chemical engineering and mass transfer studies the cobalt-catalysed reaction of sulfite to sulfate has been intensively investigated [Scheme 5, (1)].[13,14,44–46,53,55] Mostly, oxygen and its consumption is indicated by ruthenium complexes and their fluorescence abilities as mentioned above by LIF. Mixing of the sulfite solution with the cobalt(II) or copper(II) catalyst prior to the oxygenation leads to the formation of a defined equilibrium [Scheme 5, (2)] with a defined concentration [$HSO_3^{\cdot}$] [Scheme 5, (3)]. In the first step of the reaction with O_2 [Scheme 5, (4)] a chain reaction with a feedback loop is initiated [Scheme 5, (5) and (6)]. Possible termination reactions can be omitted as first estimation and hence, the rate law for O_2 consumption can be summarised as a first-order law in [O_2] [Scheme 5, (7)].[56–58]

$$0.5\,O_2 + SO_3^{2-} \overset{Co(2+)}{\rightleftharpoons} SO_4^{2-} \quad (1)$$

$$Me^{(z+1)+} + HSO_3^- \rightleftharpoons Me^{z+} + HSO_3^{\cdot} \quad (2)$$

$$[HSO_3^{\cdot}] = K\,[HSO_3^-]\,\frac{Me^{(z+1)+}}{[Me^{z+}]} \quad (3)$$

$$HSO_3^{\cdot} + O_2 \overset{k_1}{\rightarrow} HSO_5^{\cdot} \quad (4)$$

$$HSO_5^{\cdot} + HSO_3^- \overset{k_2}{\rightarrow} HSO_4^- + HSO_4^{\cdot} \quad (5)$$

$$HSO_4^{\cdot} + HSO_3^- \overset{k_3}{\rightarrow} HSO_4^- + HSO_3^{\cdot} \quad (6)$$

$$\frac{d[O_2]}{dt} = -k_1\,[HSO_3^{\cdot}]\,[O_2] \quad (7)$$

Scheme 5. Overview of chemical processes and kinetics in sulfite-sulfate oxidation.[13]

The investigation of freely rising O_2 bubbles in an aqueous solution of carboxymethyl cellulose (to increase the viscosity) shows a bubble wake with a homogeneous oxygen distribution when no chemical reaction occurs (Figure 18). With sulfite oxidation, a depletion of oxygen can be observed due to the oxygen consumption in the wake of the bubble. Kück et al. have shown that together with numerical simulation of the flow field a determination of the locally transferred amount of O_2 is possible.[13] In 2012, using a PIV-LIF method combination Kück et al. reported an enhanced mass transfer of 30 % by means of the enhancement due to a chemical reaction.[14]

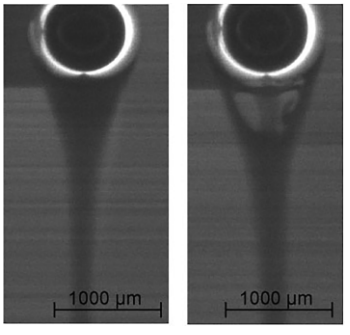

Figure 18. LIF measurements with freely rising O_2 bubbles, left: no chemical reaction, right: reaction with sulfite. Reproduced from ref.[13]

Recently, the Schlüter group investigated the influence of a superimposed sodium sulfite reaction on the concentration field after bubble contact.[54] Figure 19 illustrates the concentration field of O_2 with different concentrations of Na_2SO_3 by LIF monitoring. Here, the consumption of O_2 behind the rising bubble can directly be seen. Moreover, they demonstrated the influence of vortex structures in reactive bubbly flows on the concentration fields which can be important for the yield and selectivity of parallel-consecutive chemical reactions.[54]

3.3 Cu/O_2

As innovative approach for reactive bubbly flows, Cu/O_2 systems have been investigated in this field. Bioinorganic copper

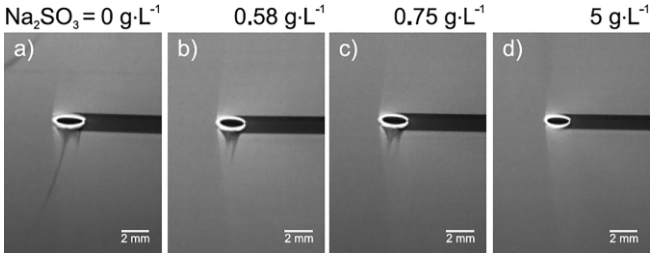

Figure 19. Qualitative oxygen concentration field around free rising bubbles with superimposed Na_2SO_3 reaction. Reproduced from ref.[54]

complexes efficiently activate molecular oxygen using nature as an archetype, e.g. tyrosinase or methane monooxygenase. Although understanding the nature and role of copper-oxygen species in enzymes is still demanding, research has made significant progress as a number of new complexes have been described and characterised with high relevance for bioinspired catalysis.[59–63]

Different types of copper enzymes provide different structural and spectroscopic features. Type 1 blue copper protein contains an active copper centre ligated by histidine, methionine and cysteine mediating electron transfer reactions in biological systems (e.g. azurin in bacteria, plastocyanin in photosynthesis). Type 2 nonblue copper protein possesses histidine and tyrosine ligands and can be found in oxygenase and oxidase reactions (e.g. galactose-oxidase in mushrooms). Type 3 proteins contain a dimeric copper centre bridged by oxygen and ligated by histidine. Those proteins promote activation and transport of oxygen (e.g. hemocyanin, catecholoxidase, tyrosinase). Tyrosinase is an essential enzyme in living organisms as it catalyses phenol oxidation which is crucial for melanin and adrenalin biosynthesis. Multicopper oxidases can oxidise organic substrates mediating the four-electron interconversion of dioxygen and water. Those type (2+3) trimers activate oxygen for oxidases (e.g. ascorbate-oxidase, laccase).

Inspired by nature, the activity and reactivity of copper oxygen intermediates in biological oxygenation and oxidation reactions were investigated by developing synthetic copper complexes mimicking enzyme oxidation abilities. Commonly Cu/O_2 complexes have been synthesised by reaction of Cu^I precursor complex with mostly weakly coordinating counterions with molecular oxygen at low temperatures (–80 °C). The used solvents are aprotic, e.g. tetrahydrofuran, dichloromethane or acetonitrile. Low oxygenation temperature increases stability of initially formed Cu_2O_2 complexes which leads to Cu/O_2 species of different stoichiometry (Figure 20). The formation of Cu_2O_2 species occurs as pseudo-first-order reaction, even at low temperatures, although there should be a higher reaction order.[64]

Possible structures of 2:1 Cu/O_2 species are side-on peroxido Cu^{II}, bis(μ-oxido) Cu^{III} as well as *trans*-1,2-μ-peroxido Cu^{II} complexes which are well-studied. The oxygen-ligated Cu^{III} species are low-spin complexes and diamagnetic. The anionic-bridged Cu^{II} centres (e.g. oxide, hydroxide) show mutual anti- or ferromagnetic coupling.[66,67] Side-on peroxido and bis(μ-oxido) intermediates are able to interconvert as they exhibit similar free energies calculated (ΔG = 0.3 kcal mol^{-1}) and thus their interconversion barrier is predicted to be very low (Scheme 6).[68] Experimental estimation of thermodynamic parameters (ΔH = –2.5 to –15.9 kJ mol^{-1} and ΔS = –8 to –84 J mol^{-1} K^{-1}) is consistent with a small isomerisation barrier.[68–71] ^{S}**P** and **O** core are differently stabilised depending on ligand system or other influences like solvent composition, temperature and counterion. Mostly only one of both ^{S}**P** and **O** species are observed as intermediate product of oxygenation.[62,63,72–74] As a result, understanding and investigation of the ^{S}**P**/**O** equilibrium is crucial for

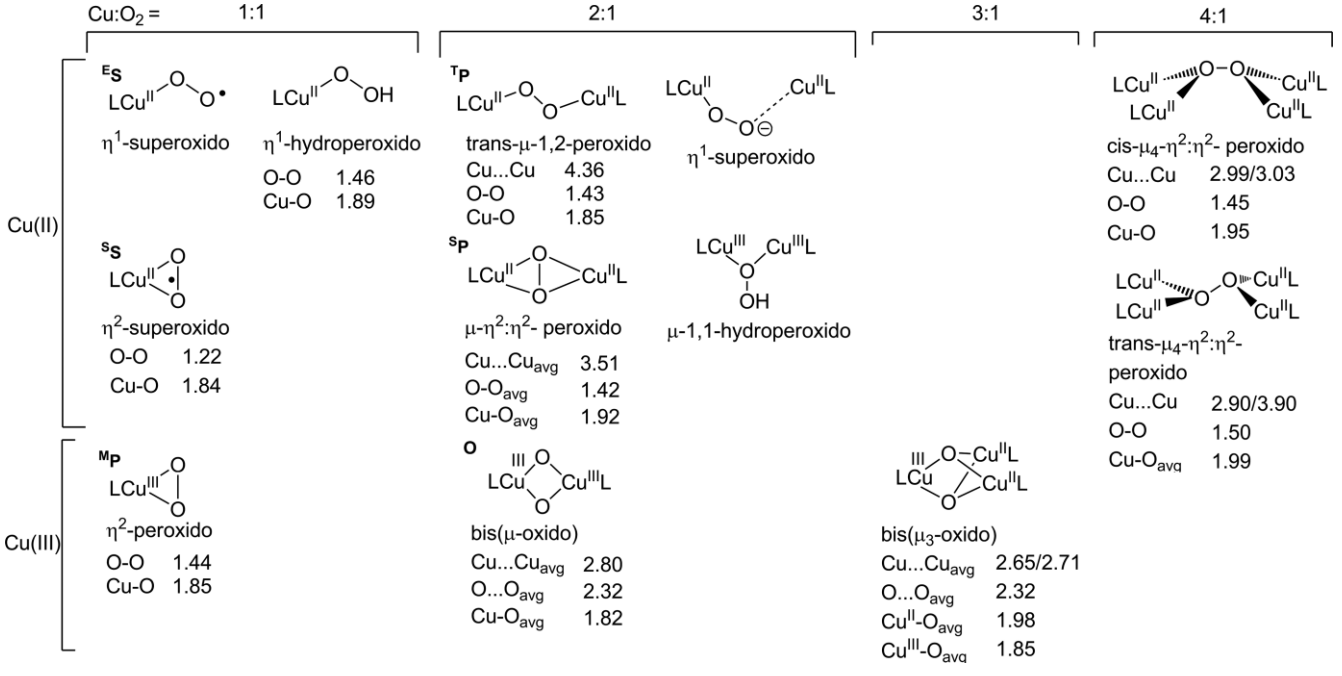

Figure 20. Cu/O_2 complexes formed by reaction of Cu^I precursor species with molecular oxygen.[65]

mechanism of dioxygen activation and consecutive oxidation abilities.

Scheme 6. Isomeric equilibrium between ^{S}**P** and **O** core.

Due to isomerisation, the side-on peroxido and bis(μ-oxido) complex show differences in their electronic structure and spectroscopic properties. Peroxido species have two absorption bands at ca. 350 nm and ca. 550 nm, whereas the oxido complex absorbs at ca. 300 nm and ca. 400 nm. Laser excitation at corresponding charge-transfer band leads to resonance Raman spectra with a characteristic peak at ca. 760 cm^{-1} for O–O stretching vibration of peroxido complex, at ca. 600 cm^{-1} for symmetrical Cu_2O_2 core expansion as well as at ca. 100 to 200 cm^{-1} for the unsymmetrical rhomb vibration of the **O** complex. The assignment of formal oxidation state performed by Cu *K*-edge X-ray absorption spectroscopy (XAS) provides the 1s to 3d transition characteristic for Cu^{II} (8979 ± 0.5 eV) and Cu^{III} (8981 ± 0.5 eV), respectively.[75,76] The electronic changes can be attributed to transformed molecular orbitals. By isomerisation of peroxido complex to oxido complex two electrons are transferred from Cu^{II} $d_{x^2-y^2}$ HOMO to σ* orbital of peroxido core, as a result of which O–O binding is cleaved homolytically and thus two μ-oxido groups are formed.[63]

The influence of ligand design on Cu_2O_2 formation is significant. Commonly, tetradentate ligands encourage the formation of *trans*-1,2-μ-peroxido complexes, whereas tri- and bidentate ligands rather stabilise **P** as well as **O** complexes. Mostly N-donor ligands are used mimicking histidine ligation in tyrosinase, e.g. amines, pyridines, guanidines. Especially guanidine ligand systems are used to investigate dioxygen activation and transfer in bubbly flow setups as discussed later (Figure 21).

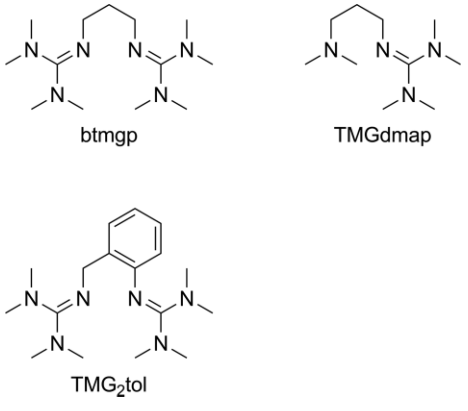

Figure 21. Ligand systems used for kinetic investigation of dioxygen activation and transfer in bubble flows.

In recent years, for both ^{S}**P** and **O** active sites there are many examples of biomimetic complexes promoting tyrosinase-related hydroxylation reactions which makes them interesting for the further investigation of competitive-consecutive reactions.[77–80] The catalytic cycle of phenol oxidation for tyrosinase model systems is proposed in Scheme 7.[81] Substrate coordination to the Cu active site is in equilibrium with the activated Cu_2O_2 species (K_{eq}). Consecutive oxidation of a phenolate is the slowest and therefore the rate-determining step of the reaction (k_{ox}). Substrate binding and catechol formation can be described as substrate-binding-kinetics to determine nucleophilicity and electrophilicity of aromatic substitution, respectively.[82]

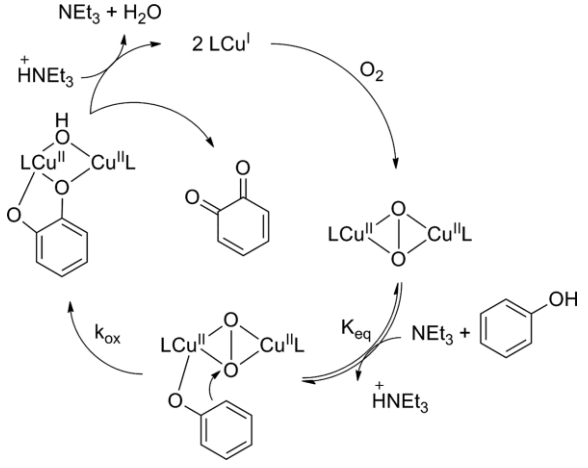

Scheme 7. Proposed reaction mechanism of catalytic phenol oxidation in presence of triethylamine.

Herres-Pawlis et al. have demonstrated the activation of dioxygen with copper btmgp complexes (Scheme 8). Guanidines are strong bases as the positive charge of the guanidinium cation is delocalised. The sterically demanding bis(guanidine) systems possess strong donation abilities to stabilise a transition metal. Their corresponding Cu^{I} complexes are air sensitive. The Cu^{I} btmgp precursor species was transformed in an **O** core complex after oxygenation at –80 °C (formation constant, 0.87 s^{-1}). The reactive Cu^{III} intermediate decayed at temperatures above –40 °C to Cu^{II} complex within seconds (decay constant, 0.01 s^{-1}). The red **O** species has characteristic absorption bands at 290 nm, 395 nm and 550 nm. At room temperature the Cu^{III} species exhibits stability in the range of milliseconds. Stopped-flow measurements of its decay at room temperature revealed a kinetic constant of 1.27 s^{-1}.[83] $^{16}O_2/^{18}O_2$ isotope Raman shifts of **O** complex from 596 cm^{-1} to 571 cm^{-1} were observed.[84]

[Cu^{I}(btmgp)I] exhibits fluorescence intensity of 60 a.u. at 405 nm at initial concentration of 10^{-2} M in acetonitrile. Quenching process due to oxygenation of [Cu^{I}(btmgp)I] at low temperature (–80 °C) leads to exponential decrease of fluorescence intensity with respect to Cu^{I} concentration after dioxygen gassing. This system can be used in a concentration range from 10^{-2} M to 10^{-9} M, e.g. in confocal characterisation measurements.[85]

The experimentally determined activation parameters of the btmgp system are in close accordance with theoretical calculations (8.8 kJ mol^{-1}). The overall energy gain of **O** core formation amounts approximately 100 kJ mol^{-1}.[86] Hydroxylation studies of btmgp-stabilised **O** complexes showed no activity with exogenous substrates (phenol as well as phenolate).

To investigate the intrinsic kinetics in a one-phase conditions, the [Cu(btmgp)I] system was tested in a liquid phase environment with a SuperFocus mixer (SFM) in 2016.[87] It was the

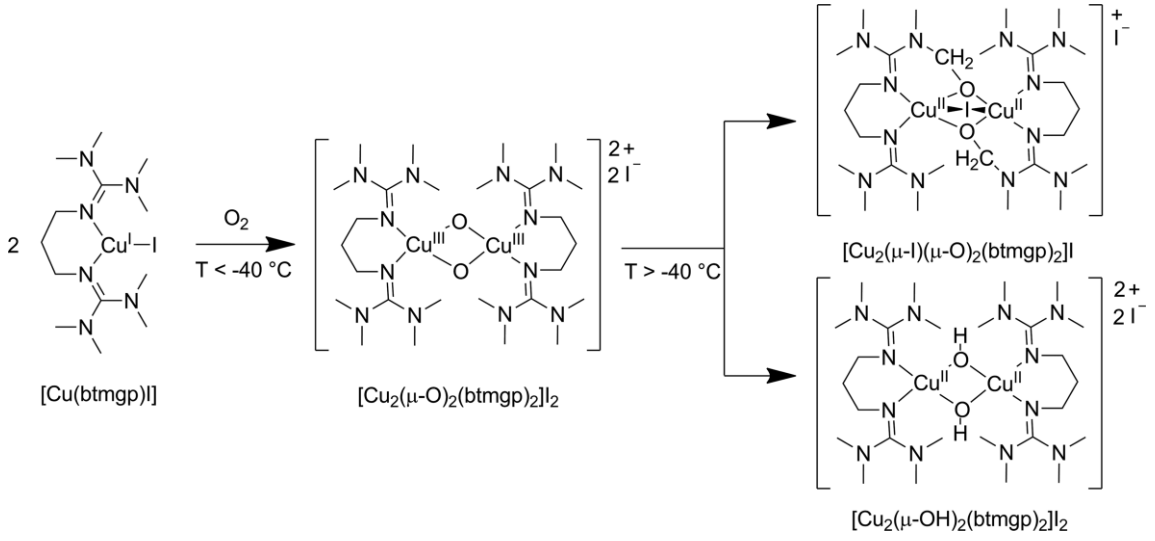

Scheme 8. Reaction process of [Cu(btmgp)I] with dioxygen in dependence of the temperature.

first time the decay of a sensitive bis(μ-oxido) dicopper species was characterised at ambient temperatures in a SFM setup. SFMs allow insights into the kinetics of a reaction system in a continuous flow system by intensive mixing of two different liquids. The SFM technology was developed by Hessel and co-workers (Figure 22).[88,89]

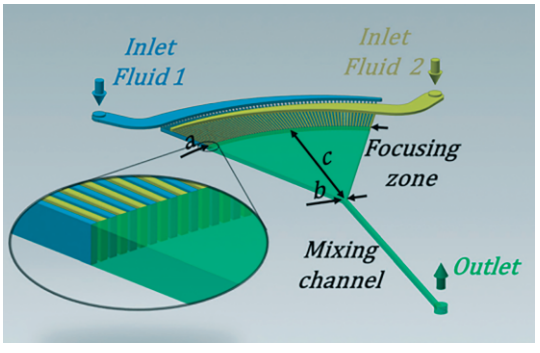

Figure 22. Schematic drawing of the SFM.[87] Reproduced with permission. Copyright 2016 The Royal Chemical Society.

Two liquids from two syringes, with flow rates controlled by a syringe pump, were mixed within a mixing chamber in a time of 10 ms. One syringe was filled with the Cu^{I} complex, dissolved in acetonitrile, the other contained an oxygen saturated acetonitrile solution. As the oxygen in this setup was dissolved and was not in the gas phase, many variables and problems with multiphase systems could be ignored. On the transparent glass mixing channel with a cross section of 0.5 mm × 0.5 mm and a total length of 200 mm a UV/Vis spectroscopy device was positioned (Figure 23).

The intermediate Cu^{III} species was followed at its characteristic band at 395 nm. With different flow rates, points at different reaction times could be achieved and evaluated to determine the rate constant of the decay at ambient temperature to be 0.87 s^{-1} which is in good accordance with stopped-flow data. The SuperFocus mixer represents a simple and fast testing system for reactions in the liquid phase that can be used to investigate the kinetics of a reaction before advancing to gas–liquid multiphase systems.

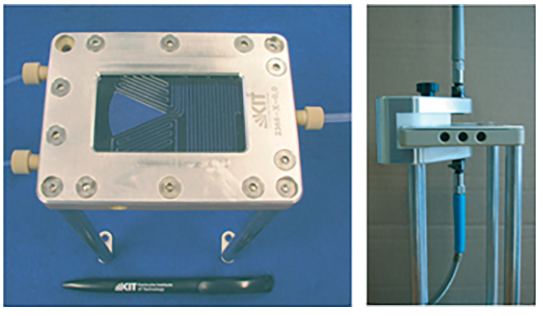

Figure 23. SFM with in- and outlet tubes (left). UV/Vis spectroscopy setup (right).[87] Reproduced with permission. Copyright 2016 The Royal Chemical Society.

The system was also used in the two-phase Taylor bubble setup by Kastens et al.[24] As the complex changes from colourless to intensive orange to green from the different species of Cu^{I}, Cu^{III} and to the Cu^{II} product (Scheme 8), imaging the reaction in the wake of the bubble was possible (Figure 24).[83]

Figure 24. [Cu(btmgp)I] with visible wake of the Cu^{III} species in Taylor bubble experiment. Reproduced from ref.[83]

Herres-Pawlis et al. have developed a similar bis(guanidine) system [Cu(TMG_2tol)I] following [Cu(btmgp)I] which reveals enhanced fluorescence abilities due to the aromatic fragment of ligand system.[90] This system is the first aromatic guanidine complex which exhibits dioxygen activation abilities. Its molecule structures were described earlier.[90] Oxygen activation and formation of the oxido complex proceeds very fast at low temperature (2.21 s^{-1}). Characteristic UV/Vis absorption bands at 290 nm and 395 nm were assigned to oxygen π_{σ^*} orbital to Cu_2O_2 and the oxygen σ^* orbital to Cu_2O_2 LMCT. The decay of

the **O** species was detected above –40 °C (0.006 s^{-1}). Activation parameters of TMG_2tol-system was experimentally determined (ΔH = 55.1 kJ mol^{-1}, ΔS = –46.6 J mol^{-1} K^{-1}). $^{16}O_2/^{18}O_2$ isotope exchange measurements with resonance Raman spectroscopy in propionitrile at –80 °C revealed a shift from 600 cm^{-1} to 572 cm^{-1} which was assigned to the breathing mode of oxido species (Figure 25). DFT calculations determined Raman modes at 616 cm^{-1} for the breathing mode, shifting to 596 cm^{-1} upon $^{16}O_2/^{18}O_2$ isotope exchange measurements.

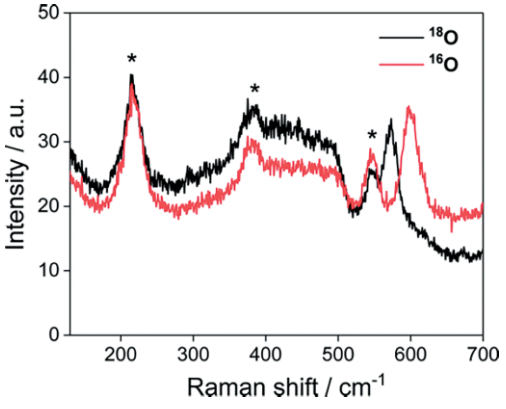

Figure 25. Raman spectrum of Cu_2O_2 species in EtCN at –80 °C. Solvent peaks are marked with *.[90]

Herres-Pawlis et al. demonstrated efficient activation of dioxygen with bis(guanidine) systems, however, those did not show any hydroxylation activities. Hybrid guanidine-stabilised oxido complexes combine different donor properties and steric encumbrance of the functional group catalysing selective hydroxylation of phenolic substrates. The Cu^I precursor complex was structurally characterised earlier.[91] Formation of **O** species $[Cu_2(\mu\text{-}O)_2(TMGdmap)_2]^{2+}$ is fast at low temperatures and exhibits high stability at –80 °C (storable for weeks). Spectral feature of the **O** core at 390 nm was observed in UV/Vis spectra. Cu *K*-edge X-ray absorption spectroscopy (XAS) measurements in THF showed pre-edge feature at 8980.5 eV assigned to 1s to 3d transition in Cu^{III} core. EXAFS analysis determined Cu–Cu distance of 2.78 Å. The characteristic absorption band in low temperature IR spectra at 651 cm^{-1} was attributed to oxido species. DFT calculations predicted asymmetrical **O** vibration of $[Cu_2(\mu\text{-}O)_2(TMGdmap)_2]^{2+}$ at 641 cm^{-1} confirming experimental measurements. However, no intermediate species was detected spectroscopically at low temperatures and/or small timescales. The decomposition of **O** species was observed at higher temperatures.[86]

DFT calculations illustrate energy data for superoxido-Cu^{II} formation with an energetically low transition state. The formation of different **P** species and finally the transformation into the corresponding bis(μ-oxido) complex proceeds downhill exhibiting a high driving force. The respective energy determined theoretically as 8.3 kJ mol^{-1} is in accordance with experimental measurements. The formation of superoxido species is rate-determining, as a result of which a pseudo-first-order reaction rate was observed. Overall stabilisation energy of **O** core formation amounts to 100 kJ mol^{-1}. This system provides the first kinetic study with full potential-surface analysis of a bioinorganic Cu/O_2 system (Figure 26).[86]

Hydroxylation abilities of TMGdmap-stabilised oxido species were observed at low temperatures (–80 °C) in THF/acetonitrile solution.[91] The reactivity study with di-*tert*-butylphenol (DTBP) exhibited the formation of corresponding catecholate in 95 % yield and *ortho*-quinone in 5 % yield leading to a hydroxylation constant of 0.3 s^{-1}. The catalytic hydroxylation study showed the conversion of DTBP into C–C coupled bisphenol in 30 % yield.[91]

The reaction system of [Cu(TMGdmap)I] is similar to [Cu(btmgp)I], as it forms an UV/Vis active oxido intermediate, which is, though, more stable than the **O** core form of [Cu(btmgp)I]. As a result, the reaction was monitored easily at room temperature with the SFM.[92] In Figure 27 the formation of the Cu^{III} intermediate at ambient temperature is shown. It took 20 min until the stable species was fully formed. Further investigations on consecutive reactions are underway at the moment.

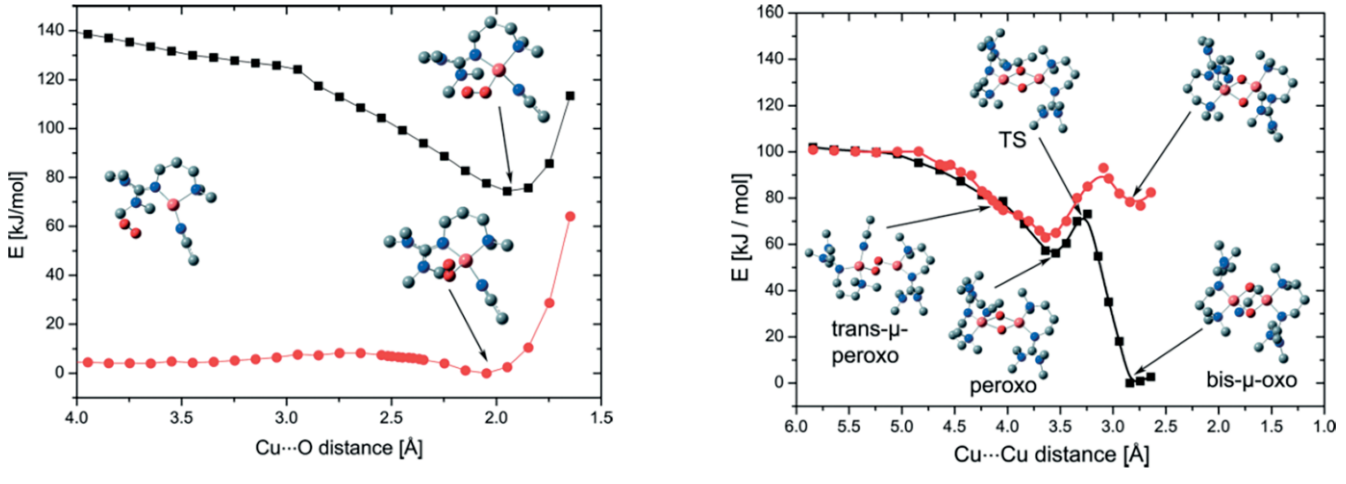

Figure 26. Energy profile of the reaction coordinate between Cu^I species and superoxido species (left) and between the superoxido and oxido species (right) (red denotes the triplet state and black the singlet state) with TPSSh/def2-TZVP.[86]

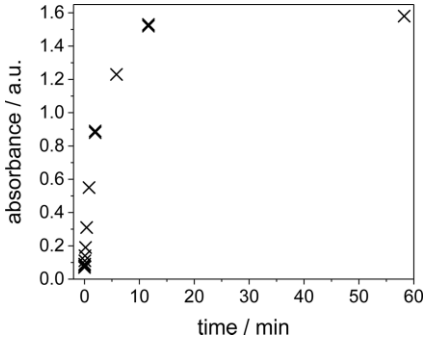

Figure 27. SFM measurement of the formation of an **O** species with the [Cu(TMGdmap)I] system in MeCN at ambient temperatures (λ_{max} = 395 nm).[92]

Another system with oxygen activation abilities provides the Cu/ammonia system. The reaction of $Cu^{I}Cl$ in aqueous ammonia leads to the formation of a copper–tetraammine complex (Scheme 9). This system showed a significant colour change in dependence on oxidation state of copper ion. In oxygen-free atmosphere the formed Cu^{I} complex remains colourless, whereas oxidation in presence of molecular oxygen leads to the corresponding deep blue Cu^{II} species.

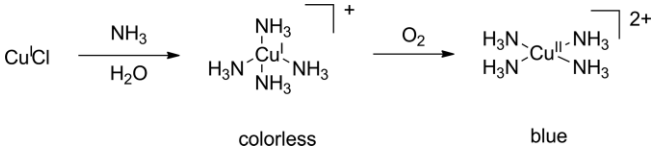

Scheme 9. Reaction of CuCl in aqueous ammonia and consecutive reaction with dioxygen.

The Cu/ammonia system was especially designed for easy, simple and fast reaction tests with oxygen. All materials can be purchased or easily synthesised with standard lab equipment. Dried CuCl is quite stable under ambient conditions. Upscaling of this system is achievable up to canister scale.

The Cu/ammonia test system was measured in a Taylor bubble column setup in 2017.[24] After the setup was calibrated and tested with CO_2 as gaseous phase (see section 2.1), the influence of a reactive system on the wake structures was investigated. Depending on the spectroscopic method and the channel size, different images were obtained (Figure 28).

Figure 28 shows the PIV-LIF images of the CO_2/water measurements, compared to the colour images and the red channel of the RGB image of the O_2/Cu/ammonia system. The wake structures, which were characterised with the CO_2/water system, represented as (a) laminar wake and (b) a toroidal vortex with the highest blue product in the wake immediately behind the bubble. Even in the turbulent wake (c) the same distributed structure was observed. Further tests with fluorescence active compounds will be characterised with PIV-LIF optical measurement techniques on a reactive system, as the fluorescence properties of ammonia solution was rather disadvantageous.

3.4 Fe/O_2

Many other natural oxidation processes using air are catalysed by iron enzymes at ambient conditions, e.g. methane monooxygenase promotes selective oxidation of methane to methanol in aqueous solution. In general, nature provides heme iron and non-heme iron active sites. Non-heme iron centres can be divided into mononuclear and dinuclear active sites. The mechanism of dioxygen-binding and -activation by non-heme iron enzymes differs significantly with the nuclearity. Whereas mononuclear enzymes (e.g. catechol dioxygenase) require a co-factor with reducing properties (e.g. pterin) in order to form reactive intermediates in oxygenation reactions.[93–95] Dinuclear systems (e.g. methane monooxygenase) make use of both iron centres to catalyse oxidation reactions of a substrate.[96,97]

Hemerythrin is the only example of a non-heme iron-based dioxygen carrier protein in living organisms. It is responsible for dioxygen transport in marine invertebrates.[98,99] This diferrous metalloprotein activates dioxygen reversibly as hydroperoxide accompanied by a two-electron reduction of O_2 to generate a diferric hydroperoxide species (Scheme 10).

For a better understanding of dioxygen activation and subsequent reactions of iron–dioxygen adducts formed, synthetic

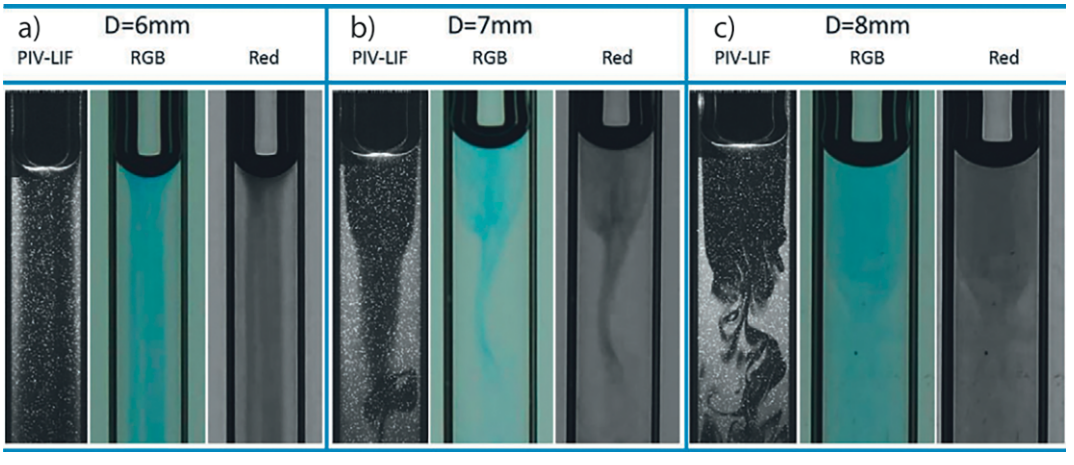

Figure 28. Wake structures of rising Taylor bubbles in different channels with (a) laminar wake, (b) toroidal wake and (c) turbulent wake. Reproduced from ref.[24]

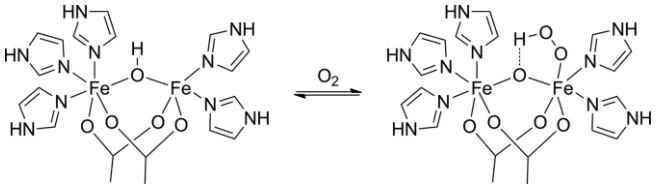

Scheme 10. Dioxygen activation at non-heme active site of hemerythrin.

model complexes were developed mimicking structural and spectroscopic features of those biomolecules. Non-heme diiron active sites in those model systems are mostly stabilised by O- and N-donor ligands. Oxygenation of diferrous centres provide a variety of oxidation states from $Fe^{II}Fe^{II}$ up to $Fe^{IV}Fe^{IV}$ (Scheme 11). Commonly, reaction of diferrous precursors with dioxygen is based on inner-sphere oxygenation mechanisms leading to various products in dependence of ligand systems as well as reaction conditions.[98,100]

Dioxygen-binding leads firstly to an Fe^{II}-Fe^{III}-superoxido intermediate followed by the formation of diiron(III)-μ-1,2-peroxido species. The stability as well as reactivity of those peroxido intermediates differ enormous depending on stabilising ligands and other influences. Most systems activate dioxygen irreversibly. Possible decomposition reaction provides disproportionation into oxido-bridged polyferric species and water or hydrogen peroxide.[101] Apart from redox activity, diiron(III)-peroxido intermediates can undergo substitution reactions of the ligand sphere.[102,103] The diferric species can also be generated by oxidation of diiron(III) precursor with H_2O_2 which is known as peroxide shunt.[103,104]

In general, Fe_2O_2 complexes are synthesised by the reaction of diferrous precursors with molecular oxygen at low temperatures. Used solvents are aprotic, e.g. nitriles, dichloromethane, tetrahydrofuran or dimethyl sulfoxide. Use of protic solvents accelerate consecutive decomposition reactions, such that in most cases no reactive intermediate like superoxido or peroxido species can be observed.[94,98,99] Formation of diiron(III)-μ-1,2-peroxido species occurs as first-order reaction with respect to the precursor concentration.

Those peroxido intermediates possess characteristic spectroscopic properties enabling to correlate such values with those of enzyme intermediates during catalysis. Formation of diiron(III)-μ-1,2-peroxido species entails absorption bands around 600 nm. Spectral features in resonance Raman spectroscopy provide values between 415 cm^{-1} and 531 cm^{-1} for Fe–O vibration modes and values between 835 cm^{-1} and 918 cm^{-1} for O–O stretching vibration of peroxido complexes. Additionally, Mößbauer spectroscopy is a useful tool to gather information of the present spin state as well as coordination geometry of the iron active sites as it shows a quadrupole doublet characteristic for Fe^{III}-high-spin centres in diiron(III)-μ-1,2-peroxido species.[99,105]

The reactive peroxido intermediate can be stabilised by bridging ligands as well as additional ligands and coordinating solvents stating the possible influence of ligand design. A well-studied ligand system for stabilisation of iron–oxygen intermediates provides the dinucleating alkoxide ligand HPTB (HPTB = *N*,*N*,*N*′,*N*′-tetrakis[2-benzimidazolylmethyl]-1,3-diamino-2-hydroxypropane) by Lippard et al. (Figure 29), bearing

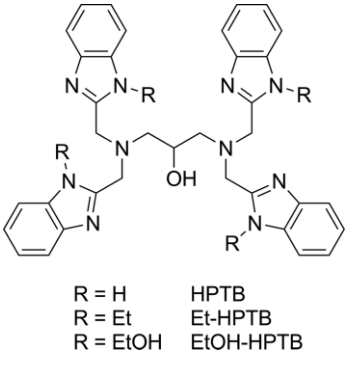

Figure 29. Ligand system HPTB and its derivatives.

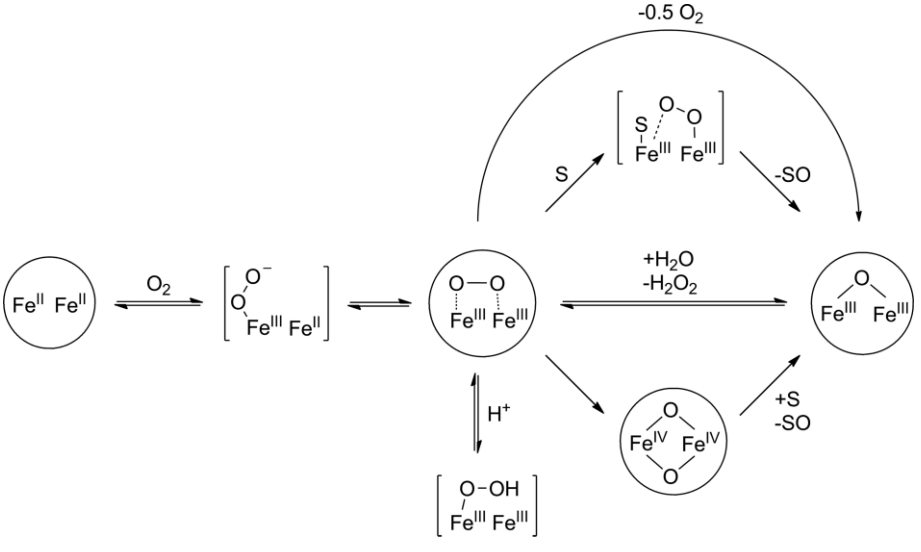

Scheme 11. Reaction of iron(II) species with dioxygen.[94]

six N-donor groups inspired by the active site of hemerythrin.[101,104]

A major goal of studying synthetic iron peroxido complexes is to mimic catalytic activity of natural enzymes mediating selective oxidation reactions of exogenous substrates. Que et al. have reported dioxygen activation abilities of iron complexes stabilised by HPTB derived ligands with benzoate as exogenous co-ligand (Scheme 12).[106] The ligand system HPTB was first synthesised and characterised by McKee et al. earlier in 1984.[107] The synthesis of the bridged yellow Fe^{II}_2 precursor complex was accomplished by conversion of the Et-HPTB ligand and an iron salt at a ratio of 2:1 in presence of benzoic acid.[106,108] Reaction with dioxygen at –60 °C in dichloromethane leads to the formation of a stable blue μ-1,2-peroxido-diiron(III)-species which binds dioxygen irreversibly. A UV/Vis absorption band at 588 nm was observed and resonance Raman features at 476 cm^{-1} and 900 cm^{-1} were observed in low-temperature studies in MeCN/MeOH which were attributed to ν_{Fe-O} and ν_{O-O}, respectively, suggesting peroxide-to-Fe^{III} LMCTs. Shifting of 16 cm^{-1} and 50 cm^{-1}, respectively, upon $^{16}O_2/^{18}O_2$ isotope exchange measurements, were in accordance with theoretically calculated modes of 455 cm^{-1} as well as 849 cm^{-1}.[108] Mößbauer parameters exhibited typical Fe^{III}-high-spin quadrupole doublet with δ = 0.52(2) mm s^{-1} and ΔE_Q = 0.72(2) mm s^{-1}, which was assigned to a symmetrically coordinating peroxide.[106] The dioxygen adduct decomposed upon warming.

The stability of the peroxido-diiron complex increased in the presence of DMSO as well as other aprotic polar solvents, as a result the peroxido intermediate can be formed and is stable for even 30 min at room temperature. Its stability is reflected in the reactivity towards exogenous substrates as the O_2 adduct showed no oxidation abilities towards DTB-H or PPh_3 at low temperatures.[108]

In 1994, Lippard et al. performed low-temperature stopped-flow kinetic studies in propionitrile to investigate the nature of the formed μ-1,2-peroxidodiiron(III) complex.[104] The activation enthalpy derived from Eyring plots based on second-order reaction rate constants (ΔH = 15.4 kJ mol^{-1}) is quite similar to those of hemerythrin (ΔH = 16.8 kJ mol^{-1}), thus indicating an addition mechanism. Difference among entropies [ΔS = –121 J mol^{-1} K^{-1}, ΔS(Hemerythrin) = –46 J mol^{-1} K^{-1}] was assigned to solvent effects.

Further investigations of Lippard et al. revealed the effect of pressure on the oxygenation rate, determined by the volume of activation (–12.8 cm^3 mol^{-1}),[101] stating the highly structured nature of transition state, which has also been reported for the oxygenation of Cu^I complexes.[109,110]

As the initially formed diferric peroxido species is metastable, Lippard et al. have found the peroxido intermediate to be completely stable at temperatures below –35 °C, at room temperature it even survived up to hours depending on the concentration. Manometric studies of the decomposition reaction revealed that this process complies with a disproportionation that either revealed a dioxygen/dinuclear ferric complex ratio of 1:2 or a dioxygen/tetranuclear ferric complex ratio of 1:1. The rate laws for the decay was ascribed to a second-order reaction with respect to the concentration of the peroxide intermediate. As a result, the authors mentioned capping as important step in oxygenation whereas the depth of coordination pocket is crucial for the decomposition reaction. Interestingly, they regard the peroxido intermediate evaluated to be highly unlikely the catalytic active species. They rather suggested the occurrence of O–O bond cleavage prior to C–H activation or an isomerisation to a more reactive species in order for efficient oxygenation of exogenous substrates.[101]

Whereas Lippard et al. described the formation of peroxido species by reaction $[Fe_2(Et\text{-}HPTB)(OBz)]^{2+}$ with dioxygen, the

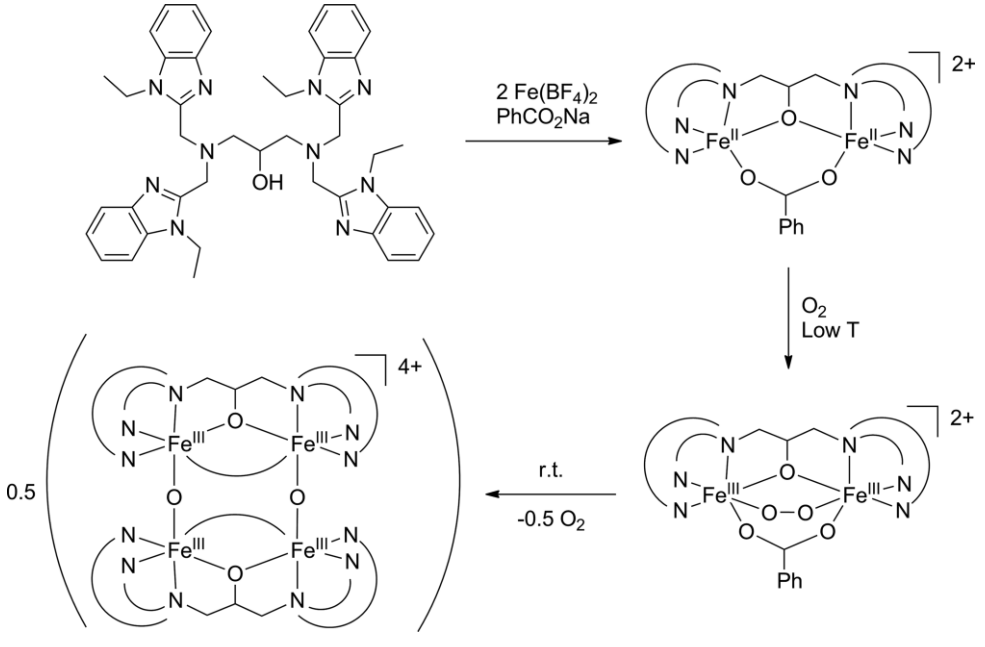

Scheme 12. Reaction of Et-HPTB stabilised iron species with dioxygen.[101]

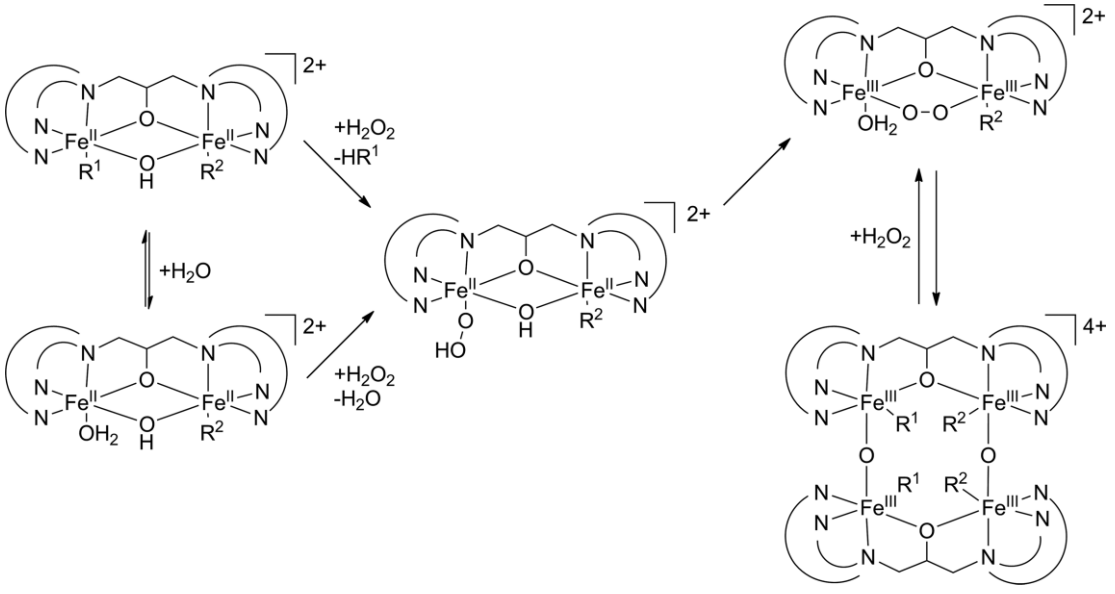

Scheme 13. Reaction of Et-HPTB stabilised iron species with hydrogen peroxide.[103]

same peroxido complex can be synthesised irreversibly by the reaction of the Fe^{III}_2 complex with hydrogen peroxide. Schindler et al. studied the reaction of hydrogen peroxide with a series of Fe^{III} precursor complexes in various solvents (Scheme 13).[103] Stopped-flow measurements showed a very fast formation of the diiron(III)-peroxido species in aqueous solution. They have found a pH-dependency of the reactivity. With increasing pH, enhanced reactivity as well as a red-shift of absorbance maxima was observed. Activation parameters were calculated at pH 3 to be ΔH = 55 kJ mol^{-1} and ΔS = 0 J mol^{-1} K^{-1}. Modification of the HPTB ligand system with *N*-EtOH groups had no influence on the oxygenation reaction with hydrogen peroxide in aqueous solution as they had similar reaction rates. The suggested two-step mechanism of the reaction consists firstly of the addition of hydrogen peroxide to an iron centre which is followed by a fast ring closure.[102] Additionally, the reaction exhibited a solvent dependency with respect to the colour, formation kinetics and stability. Absorbance maxima were shifted to higher wavelengths in methanol and even to higher wavelengths in acetonitrile. The formation of peroxido species in aqueous solution had the highest rate constant, followed by methanol, acetonitrile and DMSO. The solvent dependency is caused by the presence of water in organic solvents influencing the additional ligands due to interchange mechanisms and thus opening an additional pathway for the oxygenation of iron(III) species with H_2O_2 in organic solvents.[103] Strong ligation lead in turn to higher stability of peroxido species and slower decomposition.

In comparison with the oxygenation of diiron(II) species with dioxygen, the reaction of diiron(III) complexes with hydrogen peroxide exhibited higher stability. Due to the irreversibility of the formation of peroxido species different mechanisms should not be responsible for different lifetimes. Instead, Schindler et al. referred to stabilisation of the tetranuclear oxido-bridged iron(III) complexes resulting from decomposition reactions. Degeneration of the peroxido complex was observed in the

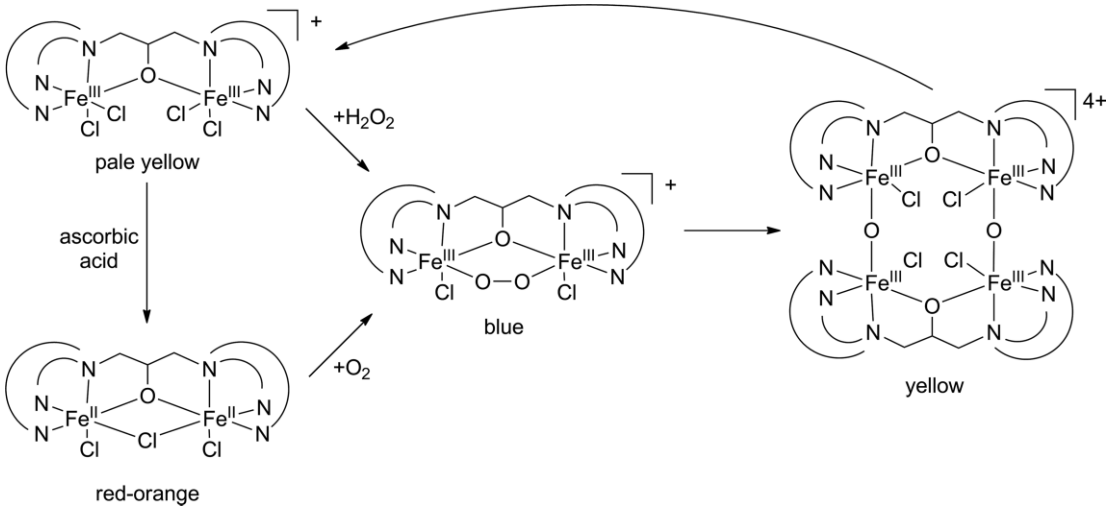

Scheme 14. Reaction of HPTB iron system with O_2 and H_2O_2.[111]

presence of an excess hydrogen peroxide explaining the higher stability. By contrast, the peroxido intermediate decomposed fast in absence of hydrogen peroxide.[103]

Recently, Schindler et al. demonstrated utilisation of the HPTB system in the activation of dioxygen in methanol to form a blue diiron peroxido intermediate with the use of chloride as anion and co-ligand (Scheme 14).[111] Decomposition of the peroxido species leads to the formation of a yellow oxygen-bridged tetrairon(III) species which has a characteristic absorption band at 375 nm.

Peroxido formation in water is critical due to very low solubility of HPTB and the corresponding Fe^{II} precursor as the decomposition product was the only observed by UV/Vis spectroscopy. Ligand modification to *N*-$C_3H_6SO_3K$-HPTB improved solubility in water, but rather no oxygenation intermediate was observed due to increased decomposition rate. Stopped-flow measurements revealed fast formation of peroxido intermediate in methanol (within seconds), which absorbs at 606 nm. Time-shifted occurrence of absorption band at 375 nm was caused by significant overlapping decomposition reaction.[111]

This system was also used in the superfocus mixer to determine the kinetics of peroxido formation, confirming those results obtained from stopped-flow measurements.

4. Systems with Fe/NO

The interaction of nitric oxide with non-heme iron complexes plays a significant role in biological processes.[112] Owing to similarities in O_2 and NO interaction with the metal active site, the development of nitrosyl adduct species may lead to more insights into the O_2 activation reaction as they possess a higher stability compared to O_2 analogues.

In nature, there are several examples of mononuclear non-heme iron proteins that are able to bind nitric oxide, e.g. soybean lipoxygenase or protocatechuate-4,5-dioxygenase.[113,114] Their reactivity towards NO has been modelled by several mononuclear ferrous complexes.[115,116]

The binding of nitric oxide to a metal active site is accompanied by stabilisation of the radical species due to a shift of electron density either towards the metal or the NO ligand. The formed metal–nitrosyl complexes can therefore be described as nitrosyl cation (NO^+) or nitroxyl anion (NO^-) derivatives leading to a linear or bent M–N–O group (Scheme 15).

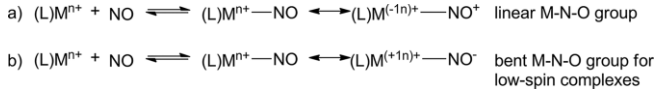

Scheme 15. Mesomeric structure in reactions.

Determination of the oxidation state of the metal in nitrosyl-iron compounds is hampered by the small energy discrepancy between metal d-orbitals and NO-π* orbitals. Therefore, Enemark and Feltham introduced the so-called Enemark–Feltham notation for nitrosyl-iron complexes by addition of metal d-electrons and NO-π* electrons.[117] NO ligands are able to adopt various configurations of transition metal binding ranging from M–N–O angles of 120° for a bent motive characteristic for low-spin complexes with singlet nitroxyl anion to 180° for a linear structure for species with nitrosyl group depending on the total number of electrons involved.

Nitric oxide binds reversibly to a ferrous active site stabilised by chelate ligands. According to Enemark and Feltham, those nitrosyl-iron species are $\{FeNO\}^7$ complexes consisting of $Fe^I(NO^+)$ $[d^7 + (\pi^*)^0]$, $Fe^{II}(NO)$ $[d^6 + (\pi^*)^1]$ and $Fe^{III}(NO^-)$ $[d^5 + (\pi^*)^2]$. $\{FeNO\}^7$ species show an $S = 3/2$ ground spin state ({NO with $S = 1/2$} + {Fe^{II} with $S = 2$}) initially observed in nitrosyl-iron proteins.[112,116,118] Those ferrous complexes were found to be stabilised by aminocarboxylate as well as pyridylmethylamine ligand systems.[115,116,119–121] Corresponding nitrosyl-iron complexes exhibit a six- or seven-coordinate structure with a quartet spin state ($S = 3/2$), which can be described as high-spin ferric active site coupled to NO^- with antiferromagnetic properties ($S = 5/2$ to $S = 1$).[116,119,120,122]

One of the first examples of aminocarboxylate-stabilised $\{FeNO\}^7$ ($S = 3/2$) complexes was shown by Chang et al. in 1987 inspired by the strength of the Fe^{II}–NO bond depending on the ligand system involved.[123] They aimed to develop suitable agents for the use in flue gas scrubbing systems. NO absorption measurements exhibited a Fe/NO stoichiometry of 1:1 assigned to a mononitrosyliron species.

Aminocarboxylate ligands (e.g. edta) stabilise the $\{FeNO\}^7$ complexes inhibiting NO release. The $\{FeNO\}^7$ moiety shows a high-spin Fe^{III} active site ($S = 5/2$) coupled to NO^- ($S = 1$) with antiferromagnetic properties.[115] MCD spectral analysis revealed an intense transition band around 22000 cm^{-1} as well as weaker bands at lower energies correlating with $S = 3/2$ ground state with identical zero field splitting.[116] XAS measurements showed a 1s to 3d pre-edge feature at 7112 eV for Fe^{III}(edta) species and a divergent pre-edge by 2 eV for Fe^{II}(edta) species, respectively, whereas the pre-edge of Fe(edta)–NO complex lied in between. Additionally, its lack of splitting was assigned to a ferric oxidation state of Fe(edta)–NO species, as only one spin-allowed state of maximum spin multiplicity ^5D is reachable. Resonance Raman spectra revealed Fe–NO-related vibrations at 1776 cm^{-1}, 517 cm^{-1} and 496 cm^{-1} for Fe(edta)–NO which were attributed to ν(NO), ν(FeN) as well as δ(FeNO). Those values were consistent with normal coordinate calculations.[116] As a result, Solomon et al. stated an electron transfer from Fe^{II} to NO as reason for ferric-NO^- complex formation. EXAFS analysis provided a bent Fe–N–O angle of Fe(edta)–NO complex close to 156°.[121]

Van Eldik et al. investigated kinetic, spectroscopic and thermodynamic properties of aqueous $\{FeNO\}^7$ ($S = 3/2$) complexes with various aminocarboxylate chelate ligands (e.g. edta, edda, hedtra, ida, oda) (Figure 30).[124]

In general, edta and analogous chelates are known to form 1:1 ferrous species, whereas mida analogues are able to form either 1:1 or 1:2 ferrous compounds. $[Fe^{II}(L)_x]$ species with 1:1 stoichiometry are quite stable in solution at pH 5 as derived from stability constants (e.g. 2×10^{14} M^{-1} for edta, 9×10^{15} M^{-1} for dtpa, 8×10^{8} M^{-1} for nta). Analogues of mida form ferrous complexes with less stability (e.g. 1×10^{12} M^{-2} for mida). The crystal structure of $[Fe^{II}(edta)]^{2-}$ exhibited a coordinated water molecule,[125,126] probably indicating a substitution mechanism

Series 1: Analogues of edta

a) 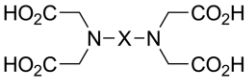

b) 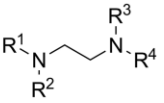

edta:	$X = (CH_2)_2$	edda	$R^1 = R^3 = H$, $R^2 = R^4 = CH_2CO_2H$
1,2-pdta	$X = CH(CH_3)\text{-}CH_2$	α-eddadp	$R^1 = R^3 = CH_2CO_2H$, $R^2 = R^4 = CH(CH_3)\text{-}CO_2H$
1,3-pdta	$X = (CH_2)_3$	β-eddadp	$R^1 = R^3 = CH_2CO_2H$, $R^2 = R^4 = (CH_2)_2CO_2H$
hpdta	$X = CH_2\text{-}CH(OH)\text{-}CH_2$	edtp	$R^1 = R^3 = R^2 = R^4 = (CH_2)_2CO_2H$
1,4-bdta	$X = (CH_2)_4$	eddhpa	$R^1 = R^3 = H$, $R^2 = R^4 = CH(o\text{-}C_6H_4OH)\text{-}CO_2H$
1,6-hdta	$X = (CH_2)_6$	hedtra	$R^1 = R^3 = R^2 = CH_2CO_2H$, $R^4 = (CH_2)_2OH$
egta	$X = ((CH_2)_2O)_2(CH_2)_2$	edds	$R^1 = R^3 = H$, $R^2 = R^4 = CH(CO_2H)\text{-}CH_2CO_2H$
cdta	X = 1,2-Cy	dtpa	$R^1 = R^3 = R^2 = CH_2CO_2H$, $R^4 = (CH_2)_2N(CH_2CO_2H)_2$

Series 2: Analogues of mida

a) 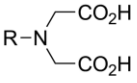

b) 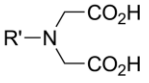

c) 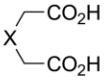

ida	R = H	edg	$R' = (CH_2)_2OH$	oda	X = O
mida	R = Me	hpida	$R' = CH_2CH(OH)\text{-}CH_3$	tda	X = S
eida	R = Et	nta	$R' = CH_2CO_2H$	glutar	$X = CH_2$
bida	R = *t*Bu	bada	$R' = (CH_2)_2CO_2H$	dipic	$X = N_{arom}$
aida	R = Ac	ada	$R' = CH_2CONH_2$		
smida	$R = CH_2SO_3H$	ceida	$R' = (CH_2)_2SCH_2CO_2H$		

Figure 30. Survey of tested chelate ligand systems.[124]

for the reaction with nitric oxide as the coordination sites are occupied.[124]

UV/Vis spectra of their corresponding nitrosyl compounds $[Fe^{II}(L)_x(NO)]$ reveal characteristic charge-transfer bands around 340 nm and 440 nm as well as one d-d transition band between 580 nm and 640 nm. While the intense CT band at 340 nm remains rather unaffected by different aminocarboxylate ligand systems, the wavelength of the low-energy CT band shifts to higher values when the d-d transition wavelength decreases. This correlation was assigned to electron density displacement between iron and nitric oxide. Simultaneously, the precursor complex is more sensitive towards oxygen depending on the ligand system (in the direction from H_2O to edta) which leads to an attenuated reversibility of NO binding (Figure 31).

Van Eldik et al. demonstrated the reversible binding of NO to $[Fe^{II}(mida)]$ by bubbling alternately NO and inert gas through the solution. For edta, an equilibrium between ferrous precursor and nitrosyl complex was observed within an hour, although the release of NO is poorer. Over a longer period of time an irreversible electron transfer from the ferrous centre to NO leads to the formation of unstable ferric nitrosyl species accompanied by dissociation of the complex to form $[Fe^{III}(edta)]^-$ and nitrous oxide. On the contrary, $[Fe^{II}(mida)]$ species exhibit no sensitivity towards oxygen, whereas the ferrous edta system shows a high oxidation rate. The same tendency was determined for mida and edta analogues (Scheme 16).

The equilibrium between the ferrous precursor species and ferrous nitrosyl complex correlates with the stability constant for nitrosyl complexes. Coordination of a chelating ligand system to the ferrous centre enhances the stability of NO binding.

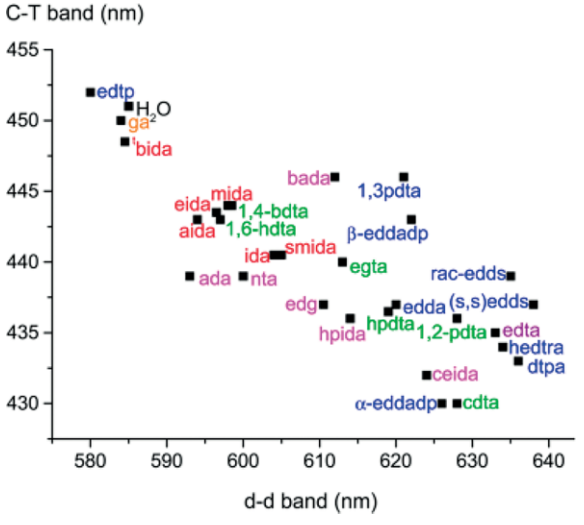

Figure 31. Correlation between C-T band and d-d band positions in the UV/Vis spectra of $[Fe^{II}(L)_x(NO)]$ complexes with L = polyamidocarboxylates. Reproduced from ref.[124]

$$[Fe^{II}(L)_x] + NO \underset{k_{off}}{\overset{k_{on}}{\rightleftharpoons}} [Fe^{II}(L)_x(NO)] \qquad K_{NO} = k_{on} / k_{off}$$

Scheme 16. Equilibrium between ferrous complex and its nitrosyl adduct.

A large number of strong donor functions in a ligand system provides high stability constants. Increased steric encumbrance of chelate ligands leads to lower K_{NO} values (Figure 32).

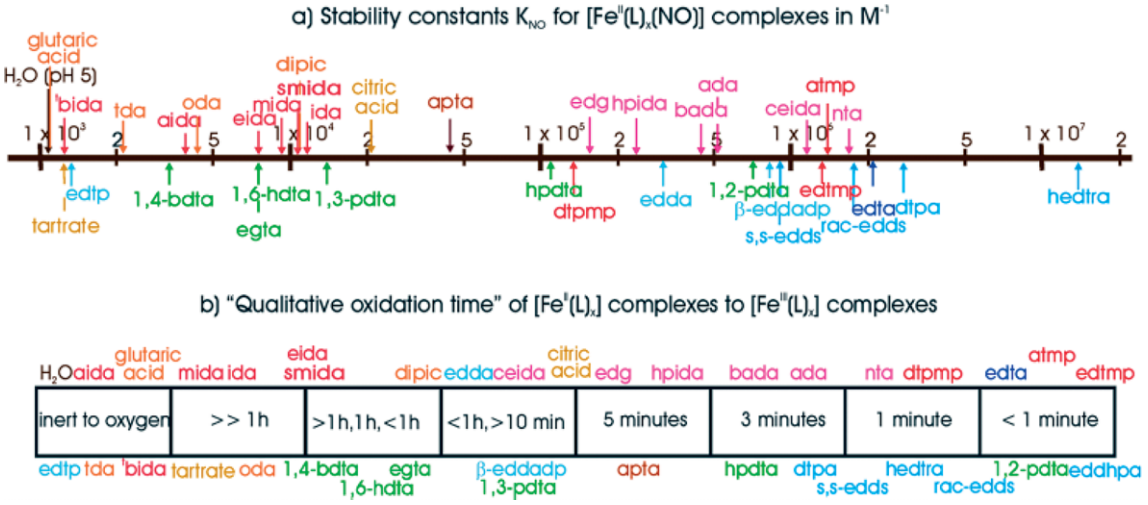

Figure 32. Correlation between K_{NO} and qualitative oxidation time of $[Fe^{II}(L)_x]$ complexes. Reproduced from ref.[124]

The stability of nitrosyl-iron complexes can also be compared to the oxygen sensitivity of corresponding precursor species (Figure 32). The "qualitative oxidation time" varies from oxygen-resistant complexes with water ligation to highly sensitive species stabilised by edta correlating an enhanced stability constant with fast oxidation processes.

The stability constants exhibit a dependency towards the charge-transfer band which was attributed to LMCT from NO to the ferrous centre (Figure 33). Nitrosyl-iron species of high stability {e.g. $[Fe(edta)(NO)]^{2-}$} revealed an LMCT band at high energy (435 nm) and a significant Fe^{III}-NO^- character of the Fe–NO bond. Less stable nitrosyl-iron compounds were suggested to have a Fe^{II}–NO characteristic Fe–NO bond. As a result, the position of the LMCT band provides directly information of the stability of nitrosyl-iron species.

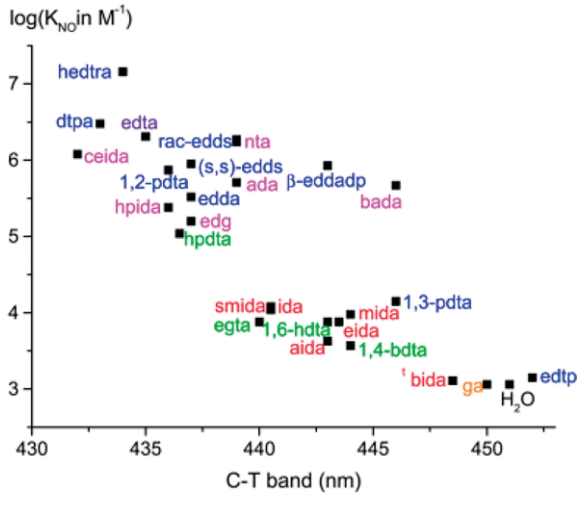

Figure 33. Correlation between the logarithmic K_{NO} values and the position of C-T band in the UV/Vis spectra of $[Fe^{II}(L)_x(NO)]$ complexes with L = polyamidocarboxylates. Reproduced from ref.[124]

In the same year, van Eldik et al. performed kinetic studies on the reaction of NO with ferrous precursor complexes.[127] Flash photolysis and pulse radiolysis revealed a high formation constant of 10^8 M^{-1} s^{-1} for the edta-stabilised species at pH 5 and room temperature. Kinetic data of the reverse release of NO were determined by stopped-flow measurements showing the fastest rate constant of 91.0 s^{-1} at room temperature for the ferrous edta complex. All other complexes exhibit significant lower rate constants for the binding of NO and as a result, lower stability constants. Respective kinetic studies of different aminocarboxylate-stabilised ferrous species are summarised by van Eldik et al.[127]

One year later, van Eldik et al. investigated the effect of temperature and pressure on the kinetics of NO binding and release on aminocarboxylate-stabilised Fe^{II} complexes.[128] Activation parameters ΔH as well as ΔS for the binding and release of NO were determined by Eyring plots. Ferrous complexes stabilised by edta, hedtra, and nta exhibit similar activation enthalpies upon reaction with NO (≈ 25 kJ mol^{-1}). Entropy values decrease slightly. The positive activation volumes were attributed to a dissociative interchange mechanism for both NO binding and release, whereas nta-stabilisation was accompanied with an associative interchange mechanism due to its six-coordinate geometry. Water exchange measurements led to higher reaction rates thus influencing the substitution process with NO. Its kinetic parameters also suggest a dissociative interchange mechanism.[129]

Recently, Klüfers et al. investigated high-spin nitrosyl-iron compounds in aqueous solution with regard to their stability (Figure 34).[130,131] The ferrous nitrosyl species can be subdivided into a low stability class and a more stable class in dependence of bubbling with inert gas through the solution. The low-stability class provides systems which lose nitric oxide within a minute under the conditions given. Stable $\{FeNO\}^7$ compounds, however, resist upon vacuum within a minute.

Synthesis of quartet-$\{FeNO\}^7$ species stabilised by different aminocarboxylate ligand systems is accomplished by reaction of ferrous sulfate heptahydrate and KOH/NaOH with corresponding free acid of ligand system in the presence of nitric oxide gas in aqueous solution. The resulting octahedral nitrosyl complex crystallises either mononuclear or as coordination

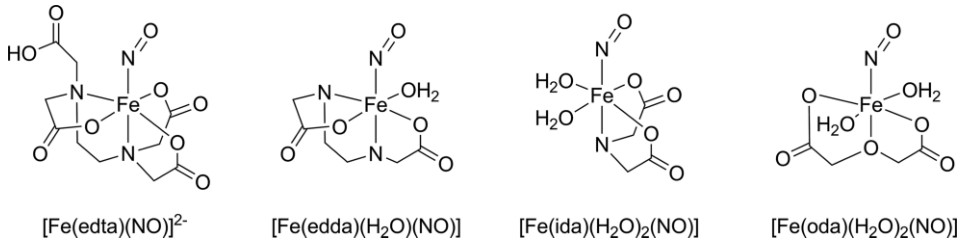

Figure 34. Molecular structures of $[Fe^{II}(L)_x(NO)]$.[131,132]

polymer. Its mother liquor showed acidic conditions before and after reaction with NO which indicates the existence of a dangling non-deprotonated carboxymethyl functional group.[130]

Particularly, the edta ligand system is used for stable solutions upon stripping with argon. The further formation of $[Fe(edta)(NO)]^{2-}$ complex leads to decreased coordination number of six and requires one edta donor to dangle freely. Stability in aqueous solution is dependent on equilibria of coordinating ligands edta, water and nitric oxide (Scheme 17). Dominating edta-containing species suppress quantitative formation of aqua-containing complexes due to their high ionic strength.[132] Upon nitric oxide absorption, more labile, easily destroyable aqua species are present in nitrosyl-iron solution. As a result, readjustment of solution equilibria leads to the formation of less stable Fe/NO complexes.

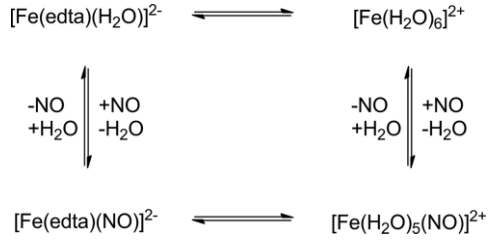

Scheme 17. Equilibria in aqueous Fe^{II}/edta/NO solutions.[130]

Further, the stability is influenced by structural features. Comparison of ferrous and ferric edta species reveals a larger Fe–O bond length for $[Fe^{II}(edta)(H_2O)]^{2-}$ (2.237 Å) than for $[Fe^{III}(edta)(H_2O)]^{-}$ (2.121 Å).[133,134] Consequently, the $Fe^{III}(NO^{-})$ species contributes significant weight to the electronic state influencing the FeNO stability in aqueous solution.

Merker et al. investigated the Fe/edta/NO system in a bubble setup.[33] For more precise results, the effects of fluid dynamics, mass transfer and the influence of a chemical reaction were analysed individually. When measuring the fluid dynamics in an impurity-free environment the measurement technique with the controlled traverse system allows a precise measurement. If components of the reactive system Fe/edta/NO are added, the terminal velocities were significantly lower. The interface was not freely movable due to the addition of the reactive Fe system, which were acting as surfactants. For tests of the gas-to-liquid mass transfer, differently prepared water solutions without the Fe complex were tested with regard to the shrinking bubble volume (Figure 35). The bubble sizes of CO_2 decreased very fast due to its higher solubility in water than NO. The volume reached lower values for degassed solutions as more gas could dissolve.

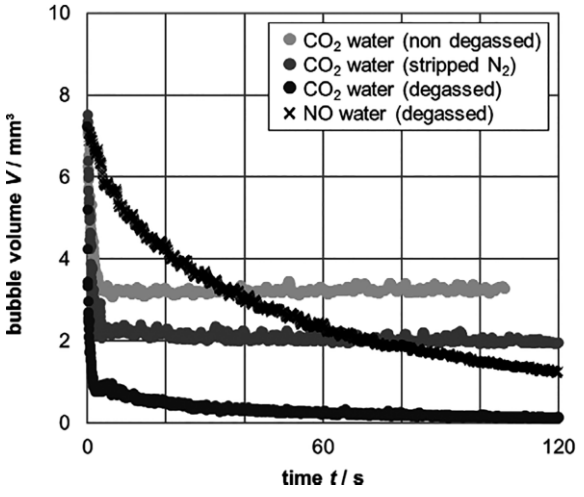

Figure 35. Bubble volume as a function of time in counter-current flow. Reproduced from ref.[33]

The mass transfer experiments with NO and the Fe(edta) reaction system showed a faster mass transfer as the NO is consumed by the reaction with the complex. The effect of the chemical system on the mass transfer is correctly described by the enhancement factor, i.e. the ratio of the mass transfer coefficients (liquid side) with and without a homogeneous chemical reaction.

Besides the Fe/edta/NO system, Hlawitschka et al. investigated iron complexes with different aminocarboxylate ligand systems and the reaction with NO in a single bubble setup with a high-speed camera.[135] The cuboidal bubble interaction apparatus with the dimensions of 90 mm × 55 mm × 115 mm has been introduced in 2005.[136] With the experimental setup the bubble rise, bubble/interface and bubble/bubble interaction with different rise velocities could be investigated, by using less than 500 mL of liquid (Figure 36). The toxic unreacted NO was destroyed by amidosulfonic acid.

The reaction around the bubbles was followed photometrically with the colour change of the complex when reacting with NO. The change in bubble size of NO without Fe complex was recorded by a high-speed camera in a counter-current flow. The shrinkage of the bubbles from sizes of 3.8 mm down to 2.1 mm was evaluated and mass transfer coefficient values in the range of 2.54×10^{-5} up to 3.56×10^{-5} ms^{-1} at 25 °C were obtained. The influence on the wake concentration of five different ligands were investigated (Table 1).

The edta and hedtra ligand systems showed the best grey-scale in the wake structure because of the higher binding stabil-

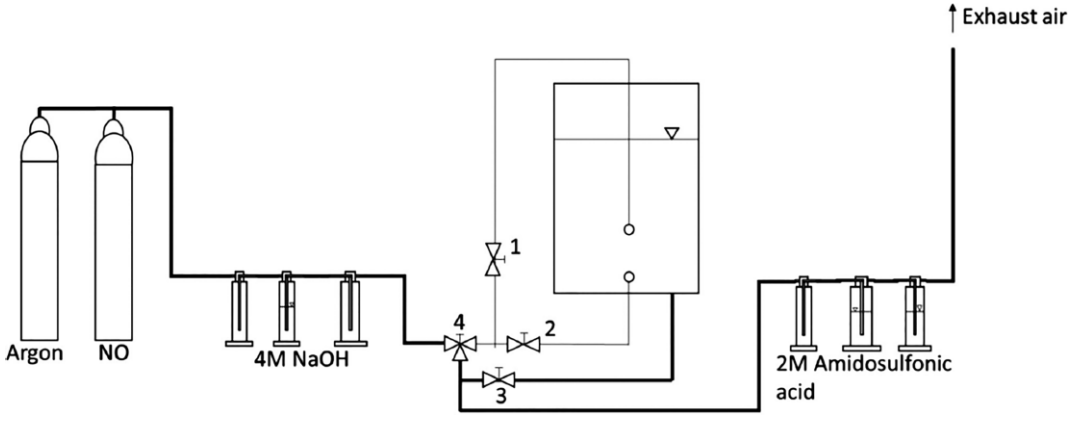

Figure 36. Sketch of experimental setup with 1–2 magnetic valves, 3 valve for degassing, 4 valve opens to exhaust air.[135] Reproduced with permission. Copyright 2017 Revue d'IFP.

Table 1. Study of different ligands and its effect on the wake concentration.[135] Reproduced with permission. Copyright 2017 Revue d'IFP.

Name (*see Appendix)	No coligand	Ligand 1	Ligand 2	Ligand 3	Ligand 4	Ligand 5
	–	oda	ida	edda	edta	hedtra
Bubble representation						
Speed where picture was taken	0.30 m s^{-1}	0.28 m s^{-1}	0.29 m s^{-1}	0.29 m s^{-1}	0.28 m s^{-1}	0.28 m s^{-1}
Size	2.8 mm	2.8 mm	2.8 mm	2.8 mm	2.9 mm	2.7 mm

ity of the NO complex, due to the higher denticity of the ligands. They concluded, that for investigating the bubble interactions under reactive mass transfer conditions, a second high-speed camera is needed to detect the bubble shape, bubble movement and bubble wake from two sides.

5. Conclusion

In this review, we have summarised the latest developments at the interface between coordination chemistry and multiphase-flow engineering. We have highlighted the dimensionality of the various measurement setups, ranging from single bubbles in capillaries via 2D cells to freely rising bubbles and bubble swarms in bubble columns. A plethora of reaction systems has been investigated in the last decades whereby a shift could be observed from studies on aqueous systems without reaction to reactive systems with potential for competitive-consecutive reactions. The first studies focussed on the basic effects of mass transfer, surfactants and bubble behaviour. The most recent studies focus on real enhancement effects where the chemical reaction accelerates mass transfer. Three main groups of coordination chemical systems have been identified as most promising for the application in reactive bubbly flows: (1) Cu/O_2 complexes, (2) Fe/O_2 complexes and (3) Fe/NO systems. Selected examples have already proven their applicability in larger apparatuses and many investigations are currently in progress. In upcoming years, the understanding of mass transfer of such reactive gases will lead to more efficient processes in industry.

Acknowledgments

The authors gratefully acknowledge the financial support provided by the German Research Foundation (DFG) within the Priority Program "Reactive Bubbly Flows", SPP 1740 (SCHL 617/12-2 and HE 5480/10-2, http://www.dfg-spp1740.de/).

Keywords: Bubbly flow · Copper · Iron · Oxygen · Kinetics

[1] D. R. Larkin, *J. Org. Chem.* **1990**, *55*, 1563–1568.
[2] M. Weber, *Chem. Eng. Technol.* **2002**, *25*, 553–558.
[3] M. Wiedemann, N. Räbiger, M. Schlüter, J. Eisenlauer, F.-X. Riener, D. Kutschera, S. Neumann, *Chem. Eng. Technol.* **2011**, *83*, 349–357.
[4] J. Hartig, G. Schuch, A. Stössel, G. Herrmann, A. Brunner, P. Zehner, O.-A. Grosskinsky, *Verfahren Zur Kontinuierlichen Herstellung von Sauerstoff Enthaltenden Verbindungen*, **1985**, DE000003328771A1.

[5] D. Kutschera, F.-X. Riener, M. Schlüter, *Verfahren Zur Herstellung von Chlorierten Carbonylverbindungen in Jet Loop Reaktoren*, **2008**, DE102006053380A1.
[6] S. Gast, J. H. Matthies, U. S. Tuttlies, U. Nieken, *Chem. Eng. Technol.* **2017**, *40*, 1445–1452.
[7] Ü. Tastan, F. Guba, D. Ziegenbalg, *Chem. Eng. Technol.* **2017**, *40*, 1418–1424.
[8] W. K. Lewis, W. G. Whitman, *Ind. Eng. Chem.* **1924**, *16*, 1215–1220.
[9] R. Higbie, *Trans. Am. Inst. Chem. Eng.* **1935**, *35*, 36–60.
[10] J. Gmehling, A. Brehm, *Grundoperationen – Lehrbuch der Technischen Chemie*, Georg Thieme Verlag, Stuttgart, **1996**.
[11] O. Bork, PhD thesis, Universität Bremen, **2006**.
[12] H. Marschall, K. Hinterberger, C. Schüler, F. Habla, O. Hinrichsen, *Chem. Eng. Sci.* **2012**, *78*, 111–127.
[13] U. D. Kück, M. Kröger, D. Bothe, N. Räbiger, M. Schlüter, H.-J. Warnecke, *Chem. Eng. Technol.* **2011**, *83*, 1084–1095.
[14] U. D. Kück, M. Schlüter, N. Räbiger, *J. Chem. Eng. Jpn.* **2012**, *45*, 708–712.
[15] A. Onea, M. Wörner, D. G. Cacuci, *Chem. Eng. Sci.* **2009**, *64*, 1416–1435.
[16] P. Peñas-López, B. van Elburg, M. A. Parrales, J. Rodríguez-Rodríguez, *Phys. Rev. Fluids* **2017**, *2*, 63602.
[17] R. Kipping, H. Kryk, E. Schleicher, M. Gustke, U. Hampel, *Chem. Eng. Technol.* **2017**, *40*, 1425–1433.
[18] P. Kováts, D. Thévenin, K. Zähringer, *Chem. Eng. Technol.* **2017**, *40*, 1434–1444.
[19] C. Fleischer, S. Becker, G. Eigenberger, *Chem. Eng. Sci.* **1996**, *51*, 1715–1724.
[20] D. Darmana, R. L. B. Henket, N. G. Deen, J. A. M. Kuipers, *Chem. Eng. Sci.* **2007**, *62*, 2556–2575.
[21] M. Yoo, S.-J. Han, J.-H. Wee, *J. Environ. Manage.* **2013**, *114*, 512–519.
[22] R. Gupta, D. F. Fletcher, B. S. Haynes, *J. Comput. Multiph. Flows* **2010**, *2*, 1–31.
[23] D. Schurr, J. Guhathakurta, S. Simon, G. Rinke, R. Dittmeyer, *Chem. Eng. Technol.* **2017**, *40*, 1400–1407.
[24] S. Kastens, J. Timmermann, F. Strassl, R. F. Rampmaier, A. Hoffmann, S. Herres-Pawlis, M. Schlüter, *Chem. Eng. Technol.* **2017**, *40*, 1494–1501.
[25] M. M. Martin, L. Lindqvist, *J. Lumin.* **1975**, *10*, 381–390.
[26] J. P. Crimaldi, *Exp. Fluids* **2008**, *44*, 851–863.
[27] M. Stöhr, J. Schanze, A. Khalili, *Exp. Fluids* **2009**, *47*, 135–143.
[28] P. Valiorgue, N. Souzy, M. El Hajem, H. Ben Hadid, S. Simoëns, *Exp. Fluids* **2013**, *54*, 1501.
[29] O. Bork, M. Schlüter, N. Räbiger, in *Lasermethoden in der Strömungsmesstechnik: 8. Fachtagung* (Eds: A. Delgado, F. Werner, B. Ruck, A. Leder, D. Dopheide), Shaker Verlag, Aachen **2000**.
[30] R. Rzehak, M. Krauß, P. Kováts, K. Zähringer, *Int. J. Multiph. Flow* **2017**, *89*, 299–312.
[31] K. Tsuchiya, H. Mikasa, T. Saito, *Chem. Eng. Sci.* **1997**, *52*, 4119–4126.
[32] K. Tsuchiya, T. Ishida, T. Saito, T. Kajishima, *Can. J. Chem. Eng.* **2003**, *81*, 647–654.
[33] D. Merker, L. Böhm, M. Oßberger, P. Klüfers, M. Kraume, *Chem. Eng. Technol.* **2017**, *40*, 1391–1399.
[34] G. Kong, K. A. Buist, E. A. J. F. Peters, J. A. M. Kuipers, *Exp. Therm. Fluid Sci.* **2018**, *93*, 186–194.
[35] D. Laupsien, A. Cockx, A. Line, *Chem. Eng. Technol.* **2017**, *40*, 1484–1493.
[36] K. Mühlfriedel, K. Baumann, *Exp. Fluids* **2000**, *28*, 2–4.
[37] R. Lindken, W. Merzkirch, *Exp. Fluids* **2002**, *33*, 814–825.
[38] C. Butler, E. Cid, A.-M. Billet, *Chem. Eng. Res. Des.* **2016**, *115*, 292–302.
[39] A. G. Cook, R. M. Tolliver, J. E. Williams, *J. Chem. Educ.* **1994**, *71*, 160.
[40] W. E. Wellman, M. E. Noble, T. Healy, *J. Chem. Educ.* **2003**, *80*, 537.
[41] N. Dietrich, K. Loubière, M. Jimenez, G. Hébrard, C. Gourdon, *Chem. Eng. Sci.* **2013**, *100*, 172–182.
[42] N. Dietrich, G. Hebrard, *Heat Mass Transfer* **2018**, *8*, 1–9.
[43] L. Yang, N. Dietrich, K. Loubière, C. Gourdon, G. Hébrard, *Chem. Eng. Sci.* **2016**, *143*, 364–368.
[44] W. Krieger, J. Lamsfuß, W. Zhang, N. Kockmann, *Chem. Eng. Technol.* **2017**, *40*, 2134–2143.
[45] A. Dani, P. Guiraud, A. Cockx, *Chem. Eng. Sci.* **2007**, *62*, 7245–7252.
[46] U. D. Kück, M. Schlüter, N. Räbiger, *Chem. Eng. Technol.* **2009**, *81*, 1599–1606.
[47] M. Jimenez, N. Dietrich, G. Hébrard, *Chem. Eng. Sci.* **2013**, *100*, 160–171.
[48] M. Roudet, A.-M. Billet, S. Cazin, F. Risso, V. Roig, *AIChE J.* **2017**, *63*, 2394–2408.
[49] M. Jimenez, N. Dietrich, A. Cockx, G. Hébrard, *AIChE J.* **2013**, *59*, 325–333.
[50] U. D. Kück, M. Schlüter, N. Räbiger, in *7th Int. Conf. Multiph, Flow*, **2010**.
[51] J. Coppeta, C. Rogers, *Exp. Fluids* **1998**, *25*, 1–15.
[52] J. Huang, T. Saito, *Chem. Eng. Sci.* **2017**, *170*, 105–115.
[53] B. Zhao, Y. Li, H. Tong, Y. Zhuo, L. Zhang, J. Shi, C. Chen, *Chem. Eng. Sci.* **2005**, *60*, 863–868.
[54] J. Timmermann, M. Hoffmann, M. Schlüter, *Chem. Eng. Technol.* **2016**, *39*, 1955–1962.
[55] M. Opletal, P. Novotný, F. J. Rejl, T. Moucha, M. Kordač, *Chem. Eng. Technol.* **2015**, *38*, 1919–1924.
[56] H. L. J. Bäckström, *Z. Phys. Chem. B* **1934**, *25*, 122–138.
[57] V. Linek, V. Vacek, *Chem. Eng. Sci.* **1981**, *36*, 1747–1768.
[58] M. Kordač, M. Opletal, V. Linek, *Chem. Eng. J.* **2011**, *167*, 314–321.
[59] P. Liebhäuser, A. Hoffmann, S. Herres-Pawlis, Reference Module in Chemistry, Molecular Sciences and Engineering, *Tyrosinase Models: Synthesis, Spectroscopy, Theory and Catalysis*, **2017**, Elsevier.
[60] E. A. Lewis, W. B. Tolman, *Chem. Rev.* **2004**, *104*, 1047–1076.
[61] C. E. Elwell, N. L. Gagnon, B. D. Neisen, D. Dhar, A. D. Spaeth, G. M. Yee, W. B. Tolman, *Chem. Rev.* **2017**, *117*, 2059–2107.
[62] E. I. Solomon, U. M. Sundaram, T. E. Machonkin, *Chem. Rev.* **1996**, *96*, 2563–2606.
[63] E. I. Solomon, D. E. Heppner, E. M. Johnston, J. W. Ginsbach, J. Cirera, M. Qayyum, M. T. Kieber-Emmons, C. H. Kjaergaard, R. G. Hadt, L. Tian, *Chem. Rev.* **2014**, *114*, 3659–3853.
[64] S. Itoh, *Curr. Opin. Chem. Biol.* **2006**, *10*, 115–122.
[65] L. M. Mirica, X. Ottenwaelder, T. D. P. Stack, *Chem. Rev.* **2004**, *104*, 1013–1046.
[66] K. T. McGregor, N. T. Watkins, D. L. Lewis, R. F. Drake, D. J. Hodgson, W. E. Hatfield, *Inorg. Nucl. Chem. Lett.* **1973**, *9*, 423–428.
[67] D. J. Hodgson, *Prog. Inorg. Chem.* **1975**, *19*, 173–241.
[68] C. J. Cramer, B. A. Smith, W. B. Tolman, *J. Am. Chem. Soc.* **1996**, *118*, 11283–11287.
[69] J. Cahoy, P. L. Holland, W. B. Tolman, *Inorg. Chem.* **1999**, *38*, 2161–2168.
[70] V. Mahadevan, M. J. Henson, E. I. Solomon, T. D. P. Stack, *J. Am. Chem. Soc.* **2000**, *122*, 10249–10250.
[71] H.-C. Liang, M. J. Henson, L. Q. Hatcher, M. A. Vance, C. X. Zhang, D. Lahti, S. Kaderli, R. D. Sommer, A. L. Rheingold, A. D. Zuberbühler, E. I. Solomon, K. D. Karlin, *Inorg. Chem.* **2004**, *43*, 4115–4117.
[72] H. Decker, R. Dillinger, F. Tuczek, *Angew. Chem. Int. Ed.* **2000**, *39*, 1591–1595; *Angew. Chem.* **2000**, *112*, 1656–1660.
[73] M. Rolff, J. Schottenheim, H. Decker, F. Tuczek, *Chem. Soc. Rev.* **2011**, *40*, 4077–4098.
[74] J. A. Halfen, S. Mahapatra, E. C. Wilkinson, S. Kaderli, V. G. Young, L. Que, A. D. Zuberbühler, W. B. Tolman, *Science* **1996**, *271*, 1397–400.
[75] L. Shan Kau, D. J. Spira-Solomon, J. E. Penner-Hahn, K. O. Hodgson, E. I. Solomon, *J. Am. Chem. Soc.* **1987**, *109*, 6433–6442.
[76] J. L. DuBois, P. Mukherjee, T. D. P. Stack, B. Hedman, E. I. Solomon, K. O. Hodgson, *J. Am. Chem. Soc.* **2000**, *122*, 5775–5787.
[77] M. Taki, S. Teramae, S. Nagatomo, Y. Tachi, T. Kitagawa, S. Itoh, S. Fukuzumi, *J. Am. Chem. Soc.* **2002**, *124*, 6367–6377.
[78] L. M. Mirica, M. Vance, D. J. Rudd, B. Hedman, K. O. Hodgson, E. I. Solomon, T. D. P. Stack, *Science* **2005**, *308*, 1890–1892.
[79] A. Company, S. Palavicini, I. Garcia-Bosch, R. Mas-Ballesté, L. Que, E. V. Rybak-Akimova, L. Casella, X. Ribas, M. Costas, *Chem. Eur. J.* **2008**, *14*, 3535–3538.
[80] B. T. Op't Holt, M. A. Vance, L. M. Mirica, D. E. Heppner, T. D. P. Stack, E. I. Solomon, *J. Am. Chem. Soc.* **2009**, *131*, 6421–6438.
[81] A. Hoffmann, C. Citek, S. Binder, A. Goos, M. Rübhausen, O. Troeppner, I. Ivanović-Burmazović, E. C. Wasinger, T. D. P. Stack, S. Herres-Pawlis, *Angew. Chem. Int. Ed.* **2013**, *52*, 5398–5401; *Angew. Chem.* **2013**, *125*, 5508–5512.
[82] C. Wilfer, P. Liebhäuser, A. Hoffmann, H. Erdmann, O. Grossmann, L. Runtsch, E. Paffenholz, R. Schepper, R. Dick, M. Bauer, M. Dürr, I. Ivanovic-Burmazovic, S. Herres-Pawlis, *Chem. Eur. J.* **2015**, *21*, 17639–17649.
[83] F. Strassl, J. Timmermann, M. Schlüter, S. Herres-Pawlis, *GIT Labor-Fachzeitschrift* **2016**, *60*, 39–41.

[84] B. Grimm-Lebsanft, C. Brett, F. Strassl, D. Rukser, M. Biednov, F. Biebl, M. Naumova, A. Hoffmann, L. Akinsinde, D. Brückner, S. Herres-Pawlis, M. Rübhausen, *Inorg. Chim. Acta* **2017**, https://doi.org/10.1016/j.ica.2017.07.010.
[85] S. Herres-Pawlis, G. Berth, V. Wiedemeier, L. Schmidt, A. Zrenner, H. J. Warnecke, *J. Lumin.* **2010**, *130*, 1958–1962.
[86] A. Hoffmann, M. Wern, T. Hoppe, M. Witte, R. Haase, P. Liebhäuser, J. Glatthaar, S. Herres-Pawlis, S. Schindler, *Eur. J. Inorg. Chem.* **2016**, *2016*, 4744–4751.
[87] D. Schurr, F. Strassl, P. Liebhäuser, G. Rinke, R. Dittmeyer, S. Herres-Pawlis, *React. Chem. Eng.* **2016**, *1*, 485–493.
[88] V. Hessel, S. Hardt, H. Löwe, F. Schönfeld, *AIChE J.* **2003**, *49*, 566–577.
[89] V. Hessel, S. Hardt, H. Löwe in *Chem. Micro Process Eng.*, Wiley-VCH, Weinheim, FRG, **2005**.
[90] F. Strassl, B. Grimm-Lebsanft, D. Rukser, F. Biebl, M. Biednov, C. Brett, R. Timmermann, F. Metz, A. Hoffmann, M. Rübhausen, S. Herres-Pawlis, *Eur. J. Inorg. Chem.* **2017**, *2017*, 3350–3359.
[91] S. Herres-Pawlis, P. Verma, R. Haase, P. Kang, C. T. Lyons, E. C. Wasinger, U. Flörke, G. Henkel, T. D. P. Stack, *J. Am. Chem. Soc.* **2009**, *131*, 1154–1169.
[92] F. Strassl, Thesis in Preparation, **2018**.
[93] E. I. Solomon, T. C. Brunold, M. I. Davis, J. N. Kemsley, S.-K. Lee, N. Lehnert, F. Neese, A. J. Skulan, Y.-S. Yang, J. Zhou, *Chem. Rev.* **2000**, *100*, 235–350.
[94] M. Costas, M. P. Mehn, M. P. Jensen, L. Que, *Chem. Rev.* **2004**, *104*, 939–986.
[95] M. M. Abu-Omar, A. Loaiza, N. Hontzeas, *Chem. Rev.* **2005**, *105*, 2227–2252.
[96] M. Merkx, D. A. Kopp, M. H. Sazinsky, J. L. Blazyk, J. Müller, S. J. Lippard, *Angew. Chem. Int. Ed.* **2001**, *40*, 2782–2807; *Angew. Chem.* **2001**, *113*, 2860–2860.
[97] M. H. Baik, M. Newcomb, R. A. Friesner, S. J. Lippard, *Chem. Rev.* **2003**, *103*, 2385–2419.
[98] E. Y. Tshuva, S. J. Lippard, *Chem. Rev.* **2004**, *104*, 987–1012.
[99] S. V. Kryatov, E. V. Rybak-Akimova, S. Schindler, *Chem. Rev.* **2005**, *105*, 2175–2226.
[100] A. L. Feig, S. J. Lippard, *Chem. Rev.* **1994**, *94*, 759–805.
[101] A. L. Feig, M. Becker, S. Schindler, R. van Eldik, S. J. Lippard, *Inorg. Chem.* **1996**, *35*, 2590–2601.
[102] R. Than, A. Schrodt, L. Westerheide, R. van Eldik, B. Krebs, *Eur. J. Inorg. Chem.* **1999**, 1537–1543.
[103] L. Westerheide, F. K. Müller, R. Than, B. Krebs, J. Dietrich, S. Schindler, *Inorg. Chem.* **2001**, *40*, 1951–1961.
[104] A. L. Feig, S. J. Lippard, *J. Am. Chem. Soc.* **1994**, *116*, 8410–8411.
[105] A. Trehoux, J. P. Mahy, F. Avenier, *Coord. Chem. Rev.* **2016**, *322*, 142–158.
[106] S. Menage, B. A. Brennan, C. Juarez-Garcia, E. Munck, L. Que, *J. Am. Chem. Soc.* **1990**, *112*, 6423–6425.
[107] V. McKee, M. Zvagulis, J. V. Dagdigian, M. G. Patch, C. A. Reed, *J. Am. Chem. Soc.* **1984**, *106*, 4765–4772.
[108] Y. Dong, S. Menage, B. A. Brennan, T. E. Elgren, H. G. Jang, L. L. Pearce, L. Que, *J. Am. Chem. Soc.* **1993**, *115*, 1851–1859.
[109] S. Goldstein, G. Czapski, R. Van Eldik, H. Cohen, D. Meyerstein, *J. Phys. Chem.* **1991**, *95*, 1282–1285.
[110] M. Becker, S. Schindler, R. van Eldik, *Inorg. Chem.* **1994**, *33*, 5370–5371.
[111] A. Miska, J. Norbury, M. Lerch, S. Schindler, *Chem. Eng. Technol.* **2017**, *40*, 1522–1526.
[112] A. L. Feig, M. T. Bautista, S. J. Lippard, *Inorg. Chem.* **1996**, *35*, 6892–6898.
[113] D. M. Arciero, J. D. Lipscomb, B. H. Huynh, T. A. Kent, E. Münck, *J. Biol. Chem.* **1983**, *258*, 14981–91.
[114] M. J. Nelson, *J. Biol. Chem.* **1987**, *262*, 12137–42.
[115] Y. Zhang, M. A. Pavlosky, C. A. Brown, T. E. Westre, B. Hedman, K. O. Hodgson, E. I. Solomon, *J. Am. Chem. Soc.* **1992**, *114*, 9189–9191.
[116] C. A. Brown, M. A. Pavlosky, T. E. Westre, Y. Zhang, B. Hedman, K. O. Hodgson, E. I. Solomon, *J. Am. Chem. Soc.* **1995**, *117*, 715–732.
[117] J. H. Enemark, R. D. Feltham, *Coord. Chem. Rev.* **1974**, *13*, 339–406.
[118] J. H. Rodriguez, Y.-M. Xia, P. G. Debrunner, *J. Am. Chem. Soc.* **1999**, *121*, 7846–7863.
[119] R. E. Shepherd, M. A. Sweetland, D. E. Junker, *J. Inorg. Biochem.* **1997**, *65*, 1–14.
[120] M. S. Ward, R. E. Shepherd, *Inorg. Chim. Acta* **1999**, *286*, 197–206.
[121] T. E. Westre, A. Di Cicco, A. Filipponi, C. R. Natoli, B. Hedman, E. I. Solomon, K. O. Hodgson, *J. Am. Chem. Soc.* **1994**, *116*, 6757–6768.
[122] C. Hauser, T. Glaser, E. Bill, T. Weyhermüller, K. Wieghardt, *J. Am. Chem. Soc.* **2000**, *122*, 4352–4365.
[123] D. Littlejohn, S. G. Chang, *Ind. Eng. Chem. Res.* **1987**, *26*, 1232–1234.
[124] T. Schneppensieper, S. Finkler, A. Czap, R. van Eldik, M. Heus, P. Nieuwenhuizen, C. Wreesmann, W. Abma, *Eur. J. Inorg. Chem.* **2001**, *2001*, 491–501.
[125] T. Mizuta, J. Wang, K. Miyoshi, *Bull. Chem. Soc. Jpn.* **1993**, *66*, 2547–2551.
[126] T. Mizuta, J. Wang, K. Miyoshi, *Inorg. Chim. Acta* **1995**, *230*, 119–125.
[127] T. Schneppensieper, A. Wanat, G. Stochel, S. Goldstein, D. Meyerstein, R. van Eldik, *Eur. J. Inorg. Chem.* **2001**, *2001*, 2317–2325.
[128] T. Schneppensieper, A. Wanat, G. Stochel, R. van Eldik, *Inorg. Chem.* **2002**, *41*, 2565–2573.
[129] L. Helm, A. E. Merbach, *Coord. Chem. Rev.* **1999**, *187*, 151–181.
[130] B. M. Aas, P. Klüfers, *Eur. J. Inorg. Chem.* **2017**, *2017*, 2313–2320.
[131] M. Wolf, P. Klüfers, *Eur. J. Inorg. Chem.* **2017**, *2017*, 2303–2312.
[132] N. H. Clark, A. E. Martell, *Inorg. Chem.* **1988**, *27*, 1297–1298.
[133] H.-M. Huang, H.-B. Yang, X.-Y. Li, F.-F. Ren, *Acta Crystallogr., Sect. E* **2009**, *65*, m87–m88.
[134] R. Meier, F. W. Heinemann, *Inorg. Chim. Acta* **2002**, *337*, 317–327.
[135] M. W. Hlawitschka, M. Oßberger, C. Backes, P. Klüfers, H.-J. Bart, *Oil Gas Sci. Technol.* **2017**, *72*, 11.
[136] P. Painmanakul, K. Loubière, G. Hébrard, M. Mietton-Peuchot, M. Roustan, *Chem. Eng. Sci.* **2005**, *60*, 6480–6491.

Received: January 31, 2018